ISSN 0038-0946, Solar System Research, 2019, Vol. 53, No. 1, pp. 30–55. © Pleiades Publishing, Inc., 2019.
Russian Text © O.V. Mingalev, O.V. Khabarova, Kh.V. Malova, I.V. Mingalev, R.A. Kislov, M.N. Mel'nik, P.V. Setsko, L.M. Zelenyi, G.P. Zank, 2019, published in Astronomicheskii Vestnik, 2019, Vol. 53, No. 1, pp. 34–60.

Modeling of Proton Acceleration in a Magnetic Island Inside the Ripple of the Heliospheric Current Sheet

O. V. Mingalev[a, *], O. V. Khabarova[b, **], Kh. V. Malova[c, d], I. V. Mingalev[a], R. A. Kislov[b, c], M. N. Mel'nik[a], P. V. Setsko[a], L. M. Zelenyi[c], and G. P. Zank[e, f]

[a] *Polar Geophysical Institute, Apatity, 184209 Russia*
[b] *Institute of Terrestrial Magnetism, Ionosphere, and Radio Wave Propagation, Russian Academy of Sciences, Moscow, 108840 Russia*
[c] *Institute of Nuclear Physics, Moscow State University, Moscow, 119234 Russia*
[d] *Space Research Institute, Russian Academy of Sciences, Moscow, 117997 Russia*
[e] *Center for Space Plasma and Aeronomic Research (CSPAR), University of Alabama, Huntsville, 35899 United States*
[f] *Department of Space Science, University of Alabama, Huntsville, 35899 United States*
** e-mail: mingalev_o@pgia.ru*
*** e-mail: habarova@izmiran.ru*

Received December 21, 2017; Revised March 1, 2018; Accepted July 25, 2018

Abstract—Crossings of the heliospheric current sheet (HCS) at the Earth's orbit are often associated with observations of anisotropic beams of energetic protons accelerated to energies from hundreds of keV to several MeV and above. A connection between this phenomenon and the occurrence of small-scale magnetic islands (SMIs) near reconnecting current sheets has recently been found. This study shows how pre-accelerated protons can be energized additionally due to oscillations of multiple SMIs inside the ripple of the reconnecting HCS. A model of the electromagnetic field of an oscillating 3D SMI with a characteristic size of ~0.001 AU is developed. A SMI is supposed to be bombarded by protons accelerated by magnetic reconnection at the HCS to energies from ~1keV to tens of keV. Numerical simulations have demonstrated that the resulting longitudinal inductive electric fields can additionally reaccelerate protons injected into a SMI. It is shown that there is a local "acceleration" region within the island in which particles gain energy most effectively. As a result, their average escape energies range from hundreds of keV to 2 MeV and above. There is almost no particle acceleration outside the region. It is shown that energies gained by protons significantly depend on the initial phase and the place of their entry into a SMI but weakly depend on the initial energy. Therefore, low-energy particles can be accelerated more efficiently than high-energy particles, and all particles can reach the total energy limit upon their escape from a SMI. It is also found that the escape velocity possesses a strong directional anisotropy. The results are consistent with observations in the solar wind plasma.

Keywords: heliospheric current sheet, magnetic islands, particle acceleration

DOI: 10.1134/S0038094619010064

INTRODUCTION

The heliospheric current sheet (HCS) is the longest-lived magnetic structure in the heliosphere. The HCS is supposed to be a continuation of the solar magnetic equator. It is a relatively thin layer of a flowing current with a thickness of about 10^4 km separating magnetic sectors, which represent large-scale regions of the oppositely directed magnetic field (sunward/anti-sunward). The HCS is surrounded by a thicker plasma layer filled with secondary current sheets, small-scale magnetic islands (SMIs), and other products of magnetic reconnection (Bemporad, 2008; Cartwright et al., 2008; Khabarova et al., 2015a; 2015b; 2016). The HCS dynamically reacts to the passage of solar wind streams of various origins, as a result of which its form is diverse and varies from large-scale waves to small ripples even in the relatively quiet heliosphere (Khabarova et al., 2015a; 2015b; 2016; 2017). Observations suggest that SMIs are formed as a result of active processes in the solar corona near the HCS. SMIs are also called magnetic bubbles, plasmoids, or bubbles, which grow, evolve, and radially expand with the solar wind along ripples of the HCS over long distances (Bemporad, 2008; Cartwright et al., 2008; Khabarova et al., 2015a; 2015b; 2016). An average size of SMIs at the Earth's orbit is ~0.001–0.01 AU, although a scatter of sizes can be large (Cartwright et al., 2008). At the same time, some SMIs are formed directly in the solar wind as a result of magnetic reconnection at the HCS or various instabilities developing in current sheets (Eastwood et al., 2002; Drake et al., 2006; Markidis et al., 2013; Greco et al., 2016; Zheng and Hu, 2018).

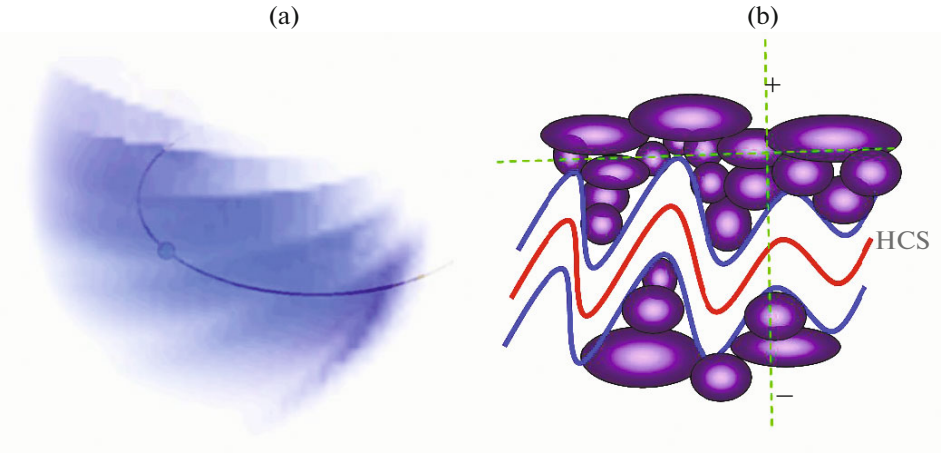

Fig. 1. HCS ripples and SMIs. (a) HCS profile reconstructed from the STELab interplanetary scintillation data. The orbit and the position of the Earth are schematically indicated as the half-circle and the dot. (b) Vertical HCS section. Magnetic islands with sizes of 0.01–0.001 AU are confined inside the HCS ripples because of the plisse shape of the HCS. The radial component of the interplanetary magnetic field outside the HCS–SMI system is directed oppositely from the two sides of the HCS (as indicated by the plus and minus signs).

Figure 1a shows relatively small-scale ripples of the HCS restored from interplanetary scintillations (see (Khabarova et al., 2015a; 2015b; 2016) and http://smei.ucsd.edu/new_smei/data&images/data&images.html). Each ripple of this sort can contain from one to several SMIs as illustrated in Fig. 1b. Figure 1b depicts the vertical section of the HCS–SMI system. The HCS triple line reflects its dividing into layers owing to magnetic reconnection, which is consistent with observations (Khabarova et al., 2015a; 2015b; 2016). The HCS often possesses a pleated form after the passage of powerful coronal mass ejections provoking the intensification of magnetic reconnection in the HCS and the excitation of different MHD waves propagating along the HCS, which in turn leads to oscillation of SMIs. In thtis work, we consider the simplest case of a single SMI confined inside a ripple of the reconnecting HCS. Khabarova et al. (2015a; 2015b; 2016) have shown that such ripples are similar to tokamaks, confining SMIs and ensuring the effectiveness of mechanisms of particle acceleration. The same occurs if a region filled with SMIs is magnetically confined anywise, for example, when magnetic cavities are formed between current sheets at fronts of various solar wind streams and the HCS. The presence of SMIs in any natural magnetic cavity bounded by strong current sheets is often accompanied by atypical enhancements in the flux of charged particles with energies up to several MeV (typically, 100 keV–1 MeV) (Khabarova et al., 2015a; 2015b; 2016). Such energetic particle flux enhancements have been called "atypical" because it was previously assumed that the process of acceleration of particles to such energies can occur only far from the Earth's orbit. It was believed that particles could be accelerated to such energies either at the Sun during flares or at coronal mass ejection-driven shocks (i.e., also near the Sun). Alternatively, it could occur at interplanetary shocks formed by streams from coronal holes at 2–3 AU. However, observations point out the local nature of energized particles as the regions in which accelerated particles are detected move together with the surrounding solar wind, which is clearly traced by several space-separated spacecraft.

A possibility of stochastic acceleration of energetic particles in SMIs due to dynamic processes was suggested by simulations (Matthaeus et al., 1984; Drake et al., 2006; Oka et al., 2010; Bian, Kontar, 2013; Zhou et al., 2015), and the theory of charged particle acceleration in merging or contracting SMIs was developed by Zank et al. (2014; 2015a; 2015b) and le Roux et al. (2015; 2016). Zank et al. (2015a; 2015b) have shown that theoretical predictions of combined particle acceleration at shocks with acceleration in SMIs downstream of the shock front is in agreement with observations of the *Voyager-2* spacecraft. The primary acceleration occurs at the shock according to the proposed combined mechanism. At the same time, the mechanism puts no constraints on the source of pre-accelerated particles trapped in merging or contracting SMIs, i.e., pre-accelerated particles can be of various nature (Zank et al., 2014; le Roux et al., 2015; 2016).

A comparison of theoretical predictions (Zank et al., 2015b) with observations has revealed an effect of two populations of accelerated particles associated with SMIs. It can be described as following: below a certain threshold energy, the relative particle acceleration is stronger for seed particles with lower energies, and, on the contrary, energetic particles with higher energies are accelerated more intensively above the

threshold energy. The mechanism proposed by (Zank et al., 2015b) explains the behavior of particles belonging to the last population. The origin of the pronounced inversion of acceleration of particles belonging to the first population has remained unknown. Obviously, a different mechanism not related to contraction or merging of SMIs can play a role here.

Let us consider possible sources of additional acceleration of particles in SMIs in the solar wind. In the absence of interplanetary shocks, pre-accelerated particles with typical energies from 1 keV to several tens of keV come to regions filled with SMIs predominantly from the quasi-regularly reconnecting HCS (Zharkova and Khabarova, 2012; 2015; Khabarova et al., 2017). In this case, the characteristic temperature of thermal protons of the solar wind is several orders of magnitude lower, varying from 1–100 eV and being ~10eV on average. One of possible mechanisms responsible for further acceleration of pre-accelerated protons near the HCS seems to be acceleration by the longitudinal electric field in a system of rather large-scale oscillating SMIs that propagate together with the solar wind along ripples of the HCS.

Collective effects of particle acceleration arising from the contraction of numerous SMIs were studied in detail in (Zank et al., 2014; 2015a; 2015b; Zhou et al., 2015; le Roux et al., 2015; 2016), suggesting stochastic particle acceleration. Regions of contraction can be observed between interacting streams of various origins as well as between the heliospheric current sheet and any approaching stream. However, the most common and natural cause of contraction/rarefaction of SMIs in the quiet solar wind is magnetohydrodynamic waves with a characteristic period from minutes to hours which propagate in the azimuthal direction along the HCS (Musielak and Suess, 1988; Wang et al., 1988; Ruderman, 1990; Dai et al., 2014). Numerical experiments show that a wavy form of the solar magnetic equator at the height of the photosphere enhances this effect and causes the occurrence of well-formed ripples of the HCS at heliocentric distances of about 1 AU (Merkin et al., 2011).

The chain of events described below seems natural in this regard. One can suggest that surface waves create oscillations of the rippled HCS and stimulate the magnetic reconnection in the HCS ripples. Particles pre-accelerated by magnetic reconnection are injected into SMIs. In the latter case, SMIs oscillate simultaneously with the oscillating HCS, which generates the inductive electric field in them. Our estimations for an arbitrarily selected island with a size of $L \sim 10^8$ m, oscillating with a period of ~10 min with an amplitude of oscillations of the magnetic field of 5 nT at 1 AU, show that the longitudinal inductive electric field can be $E_{v\|} \sim 10^{-5}$–10^{-4} V/m, while the potential electric field E_p can be 1–2 orders of magnitude lower due to the separation of charges (being no larger than 10^{-6} V/m). Therefore, the sufficiently strong longitudinal inductive electric field cannot be shielded by charge separation effects. The final energy gained by particles can increase by several orders of magnitude as a result of collective effects of particle acceleration in surrounding SMIs.

Indeed, collective effects play a dramatic role in the acceleration process in vast regions filled with dynamical SMIs as shown in (Zank et al., 2014; Zhou et al., 2015; 2015a; 2015b; le Roux et al., 2015; 2016) since they lead to the dominance of second-order Fermi acceleration over all possible energy losses in individual islands (le Roux et al., 2016).

Modeling of this large-scale and complex phenomenon in its entirety requires a huge amount of computational resources. Therefore, we propose the following approach. First, an analytical model of the electromagnetic field will be developed for in a single periodically oscillating SMI with a certain set of input parameters. The electric field is formally considered to be purely inductive in the model. Second, the built analytical model will be used to select several situations consistent with 1 AU observations of the magnetic field for numerical modeling of the particle behavior in oscillating SMIs. Next, proton trajectories will be calculated for a sufficiently representative set of initial data in the chosen magnetic fields. The set will include the initial time/oscillation phase, the initial particle acceleration point, and the initial velocity.

The modeling performed in our study has revealed an interesting and diverse picture of possible options of acceleration of protons by the longitudinal electric field generated by oscillating SMIs. The modeling results are consistent with observations and confirm the tested hypothesis.

SYSTEM GEOMETRY AND SCENARIOS OF ISLAND OSCILLATIONS

We will consider a periodically oscillating SMI which has an ellipsoid shape with semiaxes oscillating around their mean values. Note that the model is a rather simplified scheme of a SMI that can be formed as a result of magnetic reconnection of numerous current sheets surrounding the HCS. Thus, a SMI is considered as autonomous and not connected with a common current system inside the heliospheric plasma sheet, which is an undoubtedly fairly strong simplification. However, the developed model is not self-consistent. It focuses only on the processes of particle acceleration in the SMI region where electric fields are maximal. A structure of regions adjacent to a SMI as well as processes of particle injection into a SMI are

not considered. We will use the spherical coordinate system (r,α,β) with the origin in the center of the Sun, the physical basis of which is set by $\{\mathbf{h}_r,\mathbf{h}_\alpha,\mathbf{h}_\beta\}$, and components of the magnetic field in the system are denoted by B_r, B_α, B_β. We will also use the solar-magnetospheric Cartesian coordinate system GSM, the Cartesian basis of which we denote by $\{\mathbf{e}_x,\mathbf{e}_y,\mathbf{e}_z\}$, and components of the magnetic field in the system are B_x, B_y, B_z. The curvature of the magnetic field lines can be neglected at 1 AU, and it can be assumed that

$$\mathbf{e}_x = -\mathbf{h}_r,\quad \mathbf{e}_y = -\mathbf{h}_\alpha,\quad \mathbf{e}_z = \mathbf{h}_\beta,\quad B_x = -B_r,$$
$$B_y = -B_\alpha,\quad B_z = B_\beta.$$

Suppose that a large-scale ripple of the HCS is directed along $\mathbf{e}_z$, i.e., perpendicular to the ecliptic plane, which corresponds to observations. In the model, we assume that there is only one island in the ripple, which is also often takes place near the HCS.

We assume that the background electric and magnetic fields of the solar wind are uniform and steady inside HCS ripples in the undisturbed "steady" case. In the GSM coordinate system, these are as follows:

$$\mathbf{B}^{(sw)} = B_{x0}\mathbf{e}_x + B_{y0}\mathbf{e}_y,\quad \mathbf{E}^{(sw)} = E_{z0}\mathbf{e}_z. \qquad (1)$$

The solar wind speed in the GSM coordinate system upon using the SI-system is

$$\mathbf{V}^{(sw)} = \mathbf{v}_E = \frac{\left[\mathbf{E}^{(sw)}\times\mathbf{B}^{(sw)}\right]}{\left|\mathbf{B}^{(sw)}\right|^2} = \frac{E_{z0}\left(-B_{y0}\mathbf{e}_x + B_{x0}\mathbf{e}_y\right)}{\left|B_{x0}\right|^2 + \left|B_{y0}\right|^2}. \qquad (2)$$

Note that the value of the solar wind speed $V^{(sw)} = \left|\mathbf{V}^{(sw)}\right|$ varies in the range of ~250–1200 km/s according to spacecraft measurements, and its average value is about 400 km/s, i.e., the condition $V^{(sw)}/c \ll 1$ holds. The following condition is obtained from the latter and Eq. (2)

$$\frac{\left|\mathbf{E}^{(sw)}\right|}{c\left|\mathbf{B}^{(sw)}\right|} = \frac{\left|E_{z0}\right|}{c\sqrt{\left|B_{x0}\right|^2 + \left|B_{y0}\right|^2}} \ll 1.$$

At the next step we employ the coordinate system K' with axes parallel to the axes of the GSM coordinate system, moving with the solar wind speed $\mathbf{V}^{(sw)}$. There is no electric field according to the Lorentz transformation formulas for the fields in this reference frame: $\mathbf{E}^{(sw)'} = 0$, and the magnetic field has the following form:

$$\mathbf{B}^{(sw)'} = \frac{1}{\sqrt{1-\left(V^{(sw)}/c\right)^2}}$$
$$\times\left(1-\left(\left|\mathbf{E}^{(sw)}\right|/\left(c\left|\mathbf{B}^{(sw)}\right|\right)\right)^2\right)\mathbf{B}^{(sw)} \approx \mathbf{B}^{(sw)},$$

i.e., it is practically of the same order as the magnetic field in the GSM coordinate system. We consider a SMI moving along with the solar wind in the K'. In this system, the center of a SMI is steady, there is no electric field in the undisturbed steady case, and the magnetic field has the following form

$$\mathbf{B}(\mathbf{x}) = \mathbf{B}^{(sw)} + \mathbf{B}^{(i)}(\mathbf{x}). \qquad (3)$$

Here and elsewhere we omit the primes at the letters indicating fields. The spatially nonuniform part of the magnetic field $\mathbf{B}^{(i)}(\mathbf{x})$ is created by a closed current system inside the SMI (Grigorenko, 2016) with a current $\mathbf{j}^{(i)}(\mathbf{x})$, satisfying the Ampere equation

$$\mathrm{curl}\mathbf{B}^{(i)}(\mathbf{x}) = \mu_0\mathbf{j}^{(i)}(\mathbf{x}).$$

The geometry of the problem is shown schematically in Figure 2. Figure 2a shows the position of the island in the ripple of the pleated HCS. Figure 2b presents the general view of the SMI and the coordinate system. The X axis is directed sunward against the direction of the solar wind propagation. Figure 2c shows the cross section of the SMI oscillating with the period Θ by the plane $\{x = 0\}$ at times $t = 0, \Theta/4, 3\Theta/4$, corresponding to the initial position, the maximal contraction, and the maximal expansion. The SMI is elongated along the coordinate (X) due to the presence of the dominant direction of the solar wind propagation, and oscillations occur in the transverse direction (YZ). In the general case, a bubble represents a structure confined by current sheets from the two opposite sides, also assuming that the SMI is adjacent to other SMIs above and below (see the geometry in Figure 2a). In this case, the electric current flows along the HCS from the both sides of the SMI in the opposite direction as shown in Figures 2a and 2c.

Figure 3 shows the distribution of the absolute value of the normalized magnetic field of the island $\left|\mathbf{B}^{(i)}(x=0,y,z,t)\right|/B_{x0}$ in the plane $\{x = 0\}$ for the oscillation phases $\tau = 0, \Theta/8, \Theta/4$.

Let us consider a system of equations that describes slow large-scale processes in a collisionless plasma (with a characteristic time change of the order of 10 min). We will use it to analyze a possible scenario of oscillations of a SMI in the solar wind near the Earth's orbit. It is known that there are two types of basic ions in the solar wind: H^+ protons and He^{2+} α-particles. The characteristic abundance of the fraction of α-particles n_α/n_e is 5%, but near the HCS the number of α-particles is significantly reduced, therefore these can be neglected in approximate estimates.

The collisionless plasma is described by a nonrelativistic system of Vlasov–Maxwell equations on small

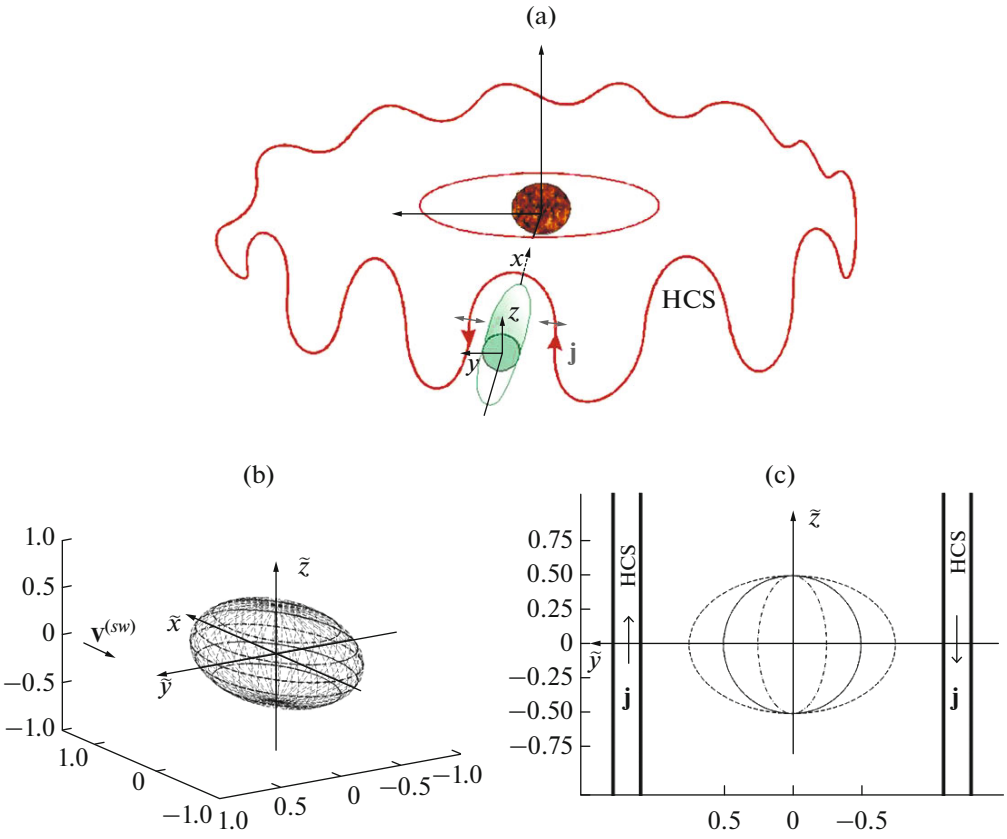

Fig. 2. Topology of the numerical experiment. (a) Schematic position of the SMI in the ripple of the HCS. (b) General view of the island and the coordinate system. (c) Cut of the island by the plane $\{x = 0\}$ for different phases of oscillations. $\tau = 0$ corresponds to the solid line, $\tau = \Theta/4$ stands for the dash-dotted line, and $\tau = 3\Theta/4$ corresponds to the dashed line.

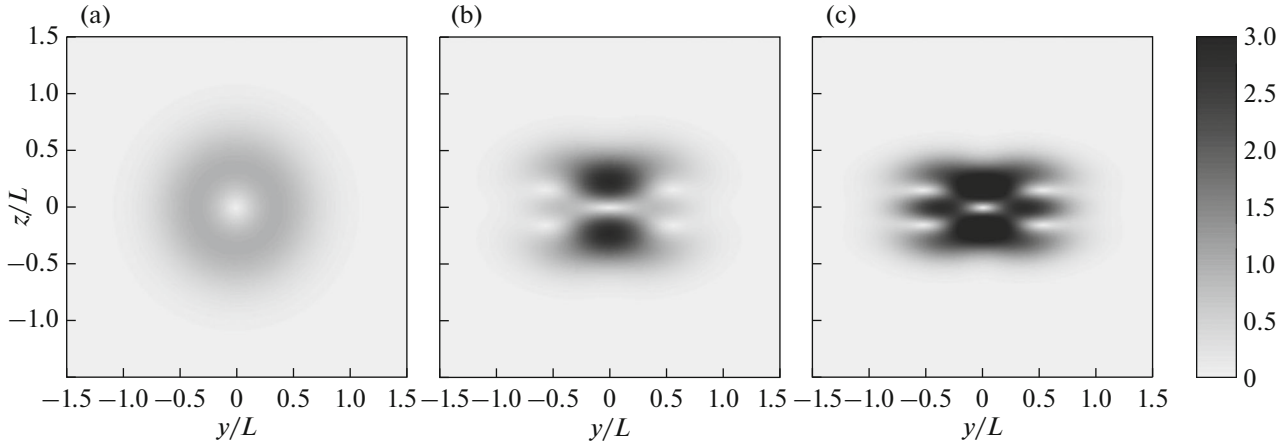

Fig. 3. Modulus of the normalized magnetic field of the island $\left|\mathbf{B}^{(i)}(x = 0, y, z, t)\right| / B_{x0}$ in the $\{x = 0\}$ plane for different phases of oscillations: (a) $\tau = 0$, (b) $\tau = \Theta/8$, and (c) $\tau = \Theta/4$.

spatial scales of the order of the Debye electron length. We denote the scalar and vector products of vectors in the space $\mathbb{R}^3$ by $(\mathbf{a},\mathbf{b})$ and $[\mathbf{a}\times\mathbf{b}]$, and the dyadic tensor with Cartesian components $(\mathbf{a}\otimes\mathbf{b})_{k,l}=a_k b_l$ formed by these vectors by $\mathbf{a}\otimes\mathbf{b}$. For each plasma component (protons p^+ and electrons e^-: $\beta=p,e$), we denote the distribution function depending on time t, the spatial coordinate $\mathbf{x}=(x_1,x_2,x_3)^T\in\mathbb{R}^3$, and the velocity $\mathbf{v}=(v_1,v_2,v_3)^T\in\mathbb{R}^3$ by $f_\beta(t,\mathbf{x},\mathbf{v})$, e_β denotes the particle charge (for electrons $e_e=-e$, where e is the proton charge), m_β indicates the particle mass, $n_\beta(\mathbf{x},t)$ denotes the density, and $\mathbf{j}_\beta(\mathbf{x},t)$ stands for the current density. ε_0 and μ_0 denote the electric and magnetic constants, and $c=1/\sqrt{\varepsilon_0\mu_0}$ is the velocity of light in vacuum. The system of Vlasov–Maxwell equations can be represented as follows in the SI system:

$$\frac{\partial f_\beta}{\partial t}+\left(\mathbf{v},\frac{\partial f_\beta}{\partial\mathbf{x}}\right)+\frac{e_\beta}{m_\beta}\left(\mathbf{E}(\mathbf{x},t)+[\mathbf{v}\times\mathbf{B}(x,t)],\frac{\partial f_\beta}{\partial\mathbf{v}}\right)=0,\quad \beta=p,e, \tag{4}$$

$$n_\beta(\mathbf{x},t)=\int_{\mathbb{R}^3} f_\beta(t,\mathbf{x},\mathbf{v})\,d^3\mathbf{v},$$
$$\rho(\mathbf{x},t)=e\big(n_p(\mathbf{x},t)-n_e(\mathbf{x},t)\big), \tag{5}$$

$$\mathbf{j}_\beta(\mathbf{x},t)=e_\beta\int_{\mathbb{R}^3}\mathbf{v}f_\beta(t,\mathbf{x},\mathbf{v})\,d^3\mathbf{v},$$
$$\mathbf{j}(\mathbf{x},t)=\mathbf{j}_p(\mathbf{x},t)+\mathbf{j}_e(\mathbf{x},t), \tag{6}$$

$$\mathrm{div}\mathbf{B}(\mathbf{x},t)=0, \tag{7}$$

$$\frac{\partial\mathbf{B}(\mathbf{x},t)}{\partial t}=-\mathrm{curl}\mathbf{E}(\mathbf{x},t), \tag{8}$$

$$\mathrm{div}\mathbf{E}(\mathbf{x},t)=\rho(\mathbf{x},t)/\varepsilon_0, \tag{9}$$

$$\varepsilon_0\frac{\partial\mathbf{E}(\mathbf{x},t)}{\partial t}=\frac{1}{\mu_0}\mathrm{curl}\mathbf{B}(\mathbf{x},t)-\mathbf{j}(\mathbf{x},t). \tag{10}$$

Here, $\mathbf{E}(\mathbf{x},t)$ is the electric field vector, $\mathbf{B}(\mathbf{x},t)$ is the vector of magnetic induction, $\rho_i(\mathbf{x},t)$ and $\mathbf{j}_i(\mathbf{x},t)$ are the total charge and ion current density, and $\rho(\mathbf{x},t)$ and $\mathbf{j}(\mathbf{x},t)$ are the total charge and the total current densities. We derive the following hydrodynamic equations for the momentum flux for each plasma component $\beta=p,e$ from Vlasov equations (4):

$$\frac{\partial\mathbf{j}_\beta}{\partial t}=\frac{e_\beta}{m_\beta}\big(e_\beta n_\beta\mathbf{E}+[\mathbf{j}_\beta\times\mathbf{B}]-\mathrm{div}\hat{\mathbf{\Pi}}_\beta\big),$$
$$\hat{\mathbf{\Pi}}_\beta(\mathbf{x},t)=m_\beta\int_{\mathbb{R}^3}\mathbf{v}\otimes\mathbf{v}f_\beta(t,\mathbf{x},\mathbf{v})\,d^3\mathbf{v}, \tag{11}$$

where $\hat{\mathbf{\Pi}}_\beta(x,t)$ is the total stress tensor for particles of each β sort. $\mathrm{div}\hat{\mathbf{\Pi}}_\beta(\mathbf{x},t)$ is the divergence vector of this tensor. Cartesian components $\Pi_{\beta,k,l}(\mathbf{x},t)$ of the tensor $\hat{\mathbf{\Pi}}_\beta(\mathbf{x},t)$ and components $\big(\mathrm{div}\hat{\mathbf{\Pi}}_\beta(\mathbf{x},t)\big)_k$ of vector $\mathrm{div}\hat{\mathbf{\Pi}}_\beta(\mathbf{x},t)$ are determined by the following formulas

$$\Pi_{\beta,k,l}(\mathbf{x},t)=m_\beta\int_{\mathbb{R}^3}v_k v_l f_\beta(t,\mathbf{x},\mathbf{v})\,d^3\mathbf{v},$$
$$\big(\mathrm{div}\hat{\mathbf{\Pi}}_\beta(\mathbf{x},t)\big)_k=\sum_{l=1}^{3}\frac{\partial\Pi_{\beta,k,l}(\mathbf{x},t)}{\partial x_l}.$$

Note that the full stress tensor $\hat{\mathbf{\Pi}}_\beta(\mathbf{x},t)$ is usually represented as a sum of the inertia tensor $m_\beta n_\beta\mathbf{u}_\beta\otimes\mathbf{u}_\beta$ and the pressure tensor $\hat{\mathbf{P}}_\beta$:

$$\hat{\mathbf{\Pi}}_\beta(\mathbf{x},t)=m_\beta n_\beta(\mathbf{x},t)\,\mathbf{u}_\beta(\mathbf{x},t)\otimes\mathbf{u}_\beta(\mathbf{x},t)+\hat{\mathbf{P}}_\beta(\mathbf{x},t), \tag{12}$$

where the hydrodynamic velocity $\mathbf{u}_\beta(\mathbf{x},t)$ and the pressure tensor are defined by the following formulas:

$$\mathbf{u}_\beta(\mathbf{x},t)=\frac{\mathbf{j}_\beta(\mathbf{x},t)}{e_\beta n_\beta(\mathbf{x},t)}=\frac{1}{n_\beta(\mathbf{x},t)}\int_{\mathbb{R}^3}\mathbf{v}f_\beta(t,\mathbf{x},\mathbf{v})\,d^3\mathbf{v}, \tag{13}$$

$$\hat{\mathbf{P}}_\beta(\mathbf{x},t)=m_\beta\int_{\mathbb{R}^3}\big(\mathbf{v}-\mathbf{u}_\beta(\mathbf{x},t)\big)\otimes\big(\mathbf{v}-\mathbf{u}_\beta(\mathbf{x},t)\big)f_\beta(t,\mathbf{x},\mathbf{v})\,d^3\mathbf{v}. \tag{14}$$

It follows from Eq. (12) that the divergence of the full stress tensor $\mathrm{div}\hat{\mathbf{\Pi}}_\beta(\mathbf{x},t)$ is the sum of the volume density of the inertia force $m_\beta\mathrm{div}\big(n_\beta\mathbf{u}_\beta\otimes\mathbf{u}_\beta\big)$ and the divergence of the pressure tensor $\mathrm{div}\hat{\mathbf{P}}_\beta$:

$$\mathrm{div}\hat{\mathbf{\Pi}}_\beta=m_\beta\mathrm{div}\big(n_\beta\mathbf{u}_\beta\otimes\mathbf{u}_\beta\big)+\mathrm{div}\hat{\mathbf{P}}_\beta. \tag{15}$$

The summation of Eq. (11) with regard to (15) leads to the following equation

$$\frac{\partial\mathbf{j}}{\partial t}=\frac{e^2n_p}{m_p}\left(\mathbf{E}+[\mathbf{u}_p\times\mathbf{B}]-\frac{m_p\mathrm{div}\big(n_p\mathbf{u}_p\otimes\mathbf{u}_p\big)}{en_p}-\frac{\mathrm{div}\hat{\mathbf{P}}_p}{en_p}\right)+\frac{e^2n_e}{m_e}\left(\mathbf{E}+[\mathbf{u}_e\times\mathbf{B}]+\frac{m_e\mathrm{div}\big(n_e\mathbf{u}_e\otimes\mathbf{u}_e\big)}{en_e}+\frac{\mathrm{div}\hat{\mathbf{P}}_e}{en_e}\right)\Bigg\}, \tag{16}$$

which is often called the generalized Ohm's law. We introduce the following notation for the convenience of further analysis:

$$\left.\begin{aligned}\left(\frac{\partial \mathbf{j}}{\partial t}\right)_E &= \left(\frac{e^2 n_p}{m_p} + \frac{e^2 n_e}{m_e}\right)\mathbf{E}, \quad \left(\frac{\partial \mathbf{j}}{\partial t}\right)_B = \frac{e^2 n_e}{m_e}[\mathbf{u}_e \times \mathbf{B}] + \frac{e^2 n_p}{m_p}[\mathbf{u}_p \times \mathbf{B}], \\ \left(\frac{\partial \mathbf{j}}{\partial t}\right)_{\text{in}} &= -e\,\text{div}\left(n_p \mathbf{u}_p \otimes \mathbf{u}_p\right) + e\,\text{div}\left(n_e \mathbf{u}_e \otimes \mathbf{u}_e\right), \quad \left(\frac{\partial \mathbf{j}}{\partial t}\right)_P = \frac{e}{m_e}\text{div}\hat{\mathbf{P}}_e - \frac{e}{m_p}\text{div}\hat{\mathbf{P}}_p.\end{aligned}\right\} \tag{17}$$

Considering the latter, Eq. (16) takes the following form

$$\frac{\partial \mathbf{j}}{\partial t} = \left(\frac{\partial \mathbf{j}}{\partial t}\right)_E + \left(\frac{\partial \mathbf{j}}{\partial t}\right)_B + \left(\frac{\partial \mathbf{j}}{\partial t}\right)_{\text{in}} + \left(\frac{\partial \mathbf{j}}{\partial t}\right)_P. \tag{18}$$

It is convenient to use the decomposition of the electric field into the potential $\mathbf{E}_p(\mathbf{x},t)$ and solenoidal $\mathbf{E}_v(\mathbf{x},t)$ parts in the considered modeling domain Ω:

$$\mathbf{E}(\mathbf{x},t) = \mathbf{E}_p(\mathbf{x},t) + \mathbf{E}_v(\mathbf{x},t), \quad \mathbf{E}_p(\mathbf{x},t) = -\nabla\varphi(\mathbf{x},t), \quad \text{div}\mathbf{E}_v(\mathbf{x},t) = 0, \quad \mathbf{x} \in \Omega. \tag{19}$$

Such a decomposition is determined up to a harmonic gradient in the domain Ω of the function:

$$\mathbf{E}'_v(\mathbf{x},t) = \mathbf{E}_v(\mathbf{x},t) + \nabla w(\mathbf{x},t),$$

$$\mathbf{E}'_p(\mathbf{x},t) = -\nabla\varphi(\mathbf{x},t) - \nabla w(\mathbf{x},t),$$

$$\Delta w(\mathbf{x},t) = 0, \quad \mathbf{x} \in \Omega,$$

where $\Delta w = \text{div}\nabla w$ is the Laplace operator. To ensure the uniqueness of such a decomposition, it is necessary to use boundary conditions, which usually follow from the specifics of a considered problem.

It should be noted that SMIs observed near current sheets in the heliosphere form a highly inhomogeneous plasma system in which the magnetic field and the density oscillate in antiphase. Such a system can contain both subregions with the increased magnetic field with respect to its intensity in the surrounding solar wind and the reduced plasma pressure as well as similar subregions with the weakened magnetic field and the increased plasma pressure. In order to show that the inductive electric field generated in the system of oscillating islands can be large and is not compensated by the ambipolar electric field of charge separation, we estimate the terms in the generalized Ohm's law (16) using the following characteristic values: the amplitude of the magnetic field oscillations in the island $\Delta B \approx 5$ nT, the oscillation period $\Theta \sim 300$ s, the island size $L_0 \sim 10^8$ m, the density $n_e \approx n_p \sim 1$–10 cm^{-3} $= 10^6$–10^7 m^{-3}, the electron temperature $T_e \approx 12$ eV, and the proton temperature $T_p \approx 8$ eV. Such values of the parameters are quite typical for SMIs in the rippled HCS observed by spacecraft at 1 AU. From the quasi-neutrality condition $n_e \approx n_p$, it follows that

$$\left(\frac{\partial \mathbf{j}}{\partial t}\right)_E = \left(\frac{e^2 n_p}{m_p} + \frac{e^2 n_e}{m_e}\right)\mathbf{E} \approx \frac{e^2 n_e}{m_e}\left(1 + \frac{m_e}{m_p}\right)\mathbf{E} \approx \frac{e^2 n_e}{m_e}\mathbf{E}. \tag{20}$$

In the slow processes under consideration, the displacement current in Maxwell's equation (10) is negligible, and it goes into the Ampere's equation

$$\text{curl}\mathbf{B}(\mathbf{x},t) = \mu_0 \mathbf{j}(\mathbf{x},t). \tag{21}$$

For simplification, one can assume that the SMI is generated by two current systems with the same magnitude but oppositely directed dipole moment and with a characteristic size of a nonuniformity of the order of $L \sim 0.1L_0 \sim 10^7$ m. The estimate follows from Eq. (21):

$$\mathbf{j}(\mathbf{x},t) = \frac{\text{curl}\mathbf{B}(\mathbf{x},t)}{\mu_0} \sim \frac{\Delta B}{\mu_0 L} \sim 5\times10^{-9}\ \text{A}/\text{m}^2. \tag{22}$$

Time differentiation of Ampere equation (21) and accounting for (22) make it possible to obtain an estimate for the time derivative of the current

$$\frac{\partial \mathbf{j}}{\partial t} = \frac{1}{\mu_0}\text{curl}\frac{\partial \mathbf{B}}{\partial t} \sim \frac{\Delta B}{\mu_0 L \Delta t} \sim 10^{-11}\ \text{A}/\left(\text{m}^2\ \text{s}\right) \tag{23}$$

It follows from the quasineutrality condition $n_e \approx n_p$, formulas (13) and estimate (22) that

$$u_p - u_e \sim \frac{j}{e n_e} \sim 0.1\text{–}1\ \text{km/s}. \tag{24}$$

This estimate, taking into account together with the quasi-neutrality condition and an estimate of $u_p \sim u_e \sim V^{(sw)} \sim 400$ km/s, leads to the conclusion that the velocity of protons in the moving coordinate system is as follows:

$$u_p \approx u_e \sim V^{(sw)} \sim 100\ \text{km/s}. \tag{25}$$

Hence,

$$\left(\frac{\partial \mathbf{j}}{\partial t}\right)_B \sim 1.5\times10^{-4}\ \text{A}/(\text{m}^2\ \text{s}) \gg \frac{\partial \mathbf{j}}{\partial t}. \tag{26}$$

From (24) and (25), it follows that the third terms in each bracket in (16) are close in magnitude and

opposite in sign, i.e., their sum is very small compared with each of them:

$$\left.\begin{aligned}\left(\frac{\partial \mathbf{j}}{\partial t}\right)_{\text{in}} &= -e\,\text{div}\left(n_p\mathbf{u}_p\otimes\mathbf{u}_p\right)+e\,\text{div}\left(n_e\mathbf{u}_e\otimes\mathbf{u}_e\right)\\ &\sim \frac{2u_e j}{L}\sim 10^{-13}\text{–}10^{-12}\ \text{A}/(\text{m}^2\,\text{s})\sim\frac{\partial \mathbf{j}}{\partial t}.\end{aligned}\right\} \quad (27)$$

If we assume that the magnetic field is $B \sim 2$–10 nT, and the temperatures of electrons and protons are $T_e \approx 12$ eV and $T_p \approx 8$ eV in the quiet solar wind and in the SMI, then their characteristic gyroradius ($r_{c\beta} = V_{T\beta}/\omega_{c\beta}$) and gyroperiods ($\theta_{c\beta} = 2\pi/\omega_{c\beta}$, where $\omega_{c\beta} = |e_\beta|B/m_\beta$ is the gyrofrequency, and $V_{T\alpha} = \sqrt{eT_\alpha/m_\alpha}$ is the thermal velocity of β-particles) are $r_{cp} \approx 30$–100 km, $r_{ce} \approx 1$–4 km and $\theta_{cp} \approx 2\pi - 10\pi$ s, $\theta_{ce} \approx 0.003$–$0.02$ s, respectively. Note that in this case thermal electrons are strongly magnetized, and their pressure tensor must be gyrotropic: $\hat{\mathbf{P}}_e(\mathbf{x},t) = p_{e\perp}(\mathbf{x},t)\hat{\mathbf{I}} + \left(p_{e\parallel}(\mathbf{x},t) - p_{e\perp}(\mathbf{x},t)\right)\mathbf{b}(\mathbf{x},t)\otimes\mathbf{b}(\mathbf{x},t)$.

Here, $p_{e\perp}$ and $p_{e\parallel}$ are the orthogonal and longitudinal pressures of electrons, $\hat{\mathbf{I}}$ is the unit tensor, and $\mathbf{b}(\mathbf{x},t) = \mathbf{B}(\mathbf{x},t)/|\mathbf{B}(\mathbf{x},t)|$ is the unit vector along the magnetic field. The divergence of this tensor is given by the following formula:

$$\begin{aligned}\text{div}\hat{\mathbf{P}}_e &= \nabla p_{e\perp} + \mathbf{b}\left(\mathbf{b},\nabla\left(p_{e\parallel}-p_{e\perp}\right)\right)\\ &+ \left(p_{e\parallel}-p_{e\perp}\right)\left((\mathbf{b},\nabla)\mathbf{b}+\mathbf{b}\,\text{div}\mathbf{b}\right).\end{aligned} \quad (28)$$

The last terms in each bracket on the right side of (16) for electrons and protons can be estimated in the approximation of isotropic pressure $\hat{\mathbf{P}}_\beta \approx p_\beta\hat{\mathbf{I}}$:

$$\left.\begin{aligned}\frac{\text{div}\hat{\mathbf{P}}_e}{en_e}&\sim\frac{\nabla p_e}{en_e}=\frac{\nabla\left(en_eT_e\right)}{en_e}\sim\frac{T_e}{L}\sim 10^{-6}\ \text{V}/\text{m}\\ \frac{\text{div}\hat{\mathbf{P}}_p}{en_p}&\sim\frac{\nabla p_p}{en_p}=\frac{\nabla\left(en_pT_p\right)}{en_p}\sim\frac{T_p}{L}\sim 10^{-6}\ \text{V}/\text{m}.\end{aligned}\right\} \quad (29)$$

Therefore,

$$\begin{aligned}\left(\frac{\partial \mathbf{j}}{\partial t}\right)_P &= \frac{e}{m_e}\left(\text{div}\hat{\mathbf{P}}_e-\frac{m_e}{m_p}\text{div}\hat{\mathbf{P}}_p\right)\\ &\approx\frac{e}{m_e}\text{div}\hat{\mathbf{P}}_e\sim 10^{-6}\ \text{A}/(\text{m}^2\ \text{s})\gg\frac{\partial \mathbf{j}}{\partial t}.\end{aligned} \quad (30)$$

It follows from (23), (26), (27), (29), and (30) that for the SMI in both the steady case and the case of oscillations, the following estimates are correct:

$$\begin{aligned}\frac{\partial \mathbf{j}}{\partial t}&\approx\left(\frac{\partial \mathbf{j}}{\partial t}\right)_E+\left(\frac{\partial \mathbf{j}}{\partial t}\right)_B+\left(\frac{\partial \mathbf{j}}{\partial t}\right)_P\approx\\ &\approx\frac{e^2n_e}{m_e}\left(\mathbf{E}+[\mathbf{u}_e\times\mathbf{B}]+\frac{\text{div}\hat{\mathbf{P}}_e}{en_e}\right)\approx 0,\end{aligned} \quad (31)$$

which means that an approximate electron equilibrium (hydrostatics) takes place. As a result, we obtain the following formula for the electric field:

$$\mathbf{E}\approx-[\mathbf{u}_e\times\mathbf{B}]-\frac{\text{div}\hat{\mathbf{P}}_e}{en_e}. \quad (32)$$

Therefore, also using (28), it is possible to estimate the longitudinal (screening) component of the electric field $E_\parallel = (\mathbf{E},\mathbf{b})$, caused by charge separation:

$$\begin{aligned}E_\parallel &\approx\frac{1}{en_e}\left(\text{div}\hat{\mathbf{P}}_e,\mathbf{b}\right)\\ &=\frac{\left(\mathbf{b},\nabla p_{e\parallel}\right)+\left(p_{e\parallel}-p_{e\perp}\right)\text{div}\mathbf{b}}{en_e}\sim 10^{-6}\ \text{V}/\text{m}.\end{aligned} \quad (33)$$

On the other hand, the estimate of the maximum deviation from electroneutrality in the inhomogeneous plasma is known (see, for example, (Lifshits and Pitaevsky, 1979, p. 186)), which in the case under consideration has the following form, taking into account the designations in (5):

$$\frac{1}{n_e}\left(n_e-n_p\right)\sim\left(\frac{\lambda_{\text{De}}}{L}\right)^2, \quad (34)$$

where L is the size of the inhomogeneity, $\lambda_{\text{De}} = V_{\text{Te}}/\omega_{pe}$ is the Debye length, $\omega_{pe} = e\sqrt{n_e/(\varepsilon_0 m_e)}$ is the plasma frequency, and $V_{\text{Te}} = \sqrt{eT_e/m_e}$ is the electron thermal velocity. The characteristic values of the parameters indicated above (20) and (22), give the value of the Debye length $\lambda_{\text{De}} \sim 10$ m in the solar wind. The following equation is obtained for the potential part of the electric field $\mathbf{E}_p(\mathbf{x},t) = -\nabla\varphi(\mathbf{x},t)$ from Poisson equation (9)

$$\text{div}\mathbf{E}_p(\mathbf{x},t) = \rho(\mathbf{x},t)/\varepsilon_0.$$

We obtain the following estimate from this equation and (34):

$$\begin{aligned}E_p &\sim L\frac{\rho}{\varepsilon_0}=L\frac{en_e}{\varepsilon_0}\frac{1}{n_e}\left(n_e-n_p\right)\sim L\frac{en_e}{\varepsilon_0}\left(\frac{\lambda_{\text{De}}}{L}\right)^2\\ &=\frac{en_e}{\varepsilon_0 L}\left(\lambda_{\text{De}}\right)^2=\frac{T_e}{L}\sim 10^{-6}\ \text{V}/\text{m},\end{aligned} \quad (35)$$

which, as one can see, coincides with the estimate of the electric field appearing due to the divergence of the electron pressure tensor. Note that as follows from (35) and (32), the orthogonal part of the hydrodynamic velocity of electrons $\mathbf{u}_{e\perp}$ should be sufficiently small in the steady case.

Therefore, (33) and (35) show that the longitudinal screening electric field is $E_\parallel \sim 10^{-6}$ V/m due to order-of-magnitude charge separation in the SMI. If the

SMI oscillates, according to Faraday's equation (8), the inductive field appears

$$E_v \sim L\frac{\Delta B}{\Theta} \sim 10^7 \times \frac{5\times 10^{-9}}{100} \sim 5\times 10^{-4}\ \text{V/m}, \quad (36)$$

which is two orders of magnitude larger than the screening field, as follows from estimate (36). In this case, the part of the inductive electric field orthogonal to **B** in approximate equation (32) is compensated by the term $[\mathbf{u}_e \times \mathbf{B}]$. Summarizing, the inductive electric field generated in the oscillating SMI is sufficiently large, and the charge separation (screening) field cannot compensate it. As a result, the inductive electric field can effectively accelerate charged particles injected into SMIs.

MODEL OF THE MAGNETIC AND ELECTRIC FIELDS IN THE MAGNETIC ISLAND

Self-consistent modeling of distribution of the magnetic and electric field and plasma parameters in a SMI in the solar wind near the Earth's orbit is a large and complex problem that lies far beyond the scope of this paper. It is difficult to build a reasonable model of the potential electric field. Estimates (35), (36) show that it is approximately two orders of magnitude smaller than the inductive electric field arising due to oscillations of a SMI. Therefore, we do not take into account the potential electric field $\mathbf{E}_p(\mathbf{x},t)$ and assume that the electric field in a SMI is purely inductive in our simple analytical model. Therefore, the fields are determined by the vector potential $\mathbf{A}(\mathbf{x},t)$:

$$\begin{aligned}\mathbf{B}(\mathbf{x},t) &= B_{x0}\mathbf{e}_x + B_{y0}\mathbf{e}_y + \text{curl}\mathbf{A}(\mathbf{x},t),\\ \mathbf{E}(\mathbf{x},t) &= -\frac{\partial \mathbf{A}(\mathbf{x},t)}{\partial t}.\end{aligned} \quad (37)$$

In this case, the electroneutrality condition is formally satisfied:

$$\text{div}\mathbf{E}(\mathbf{x},t) = 0, \quad (38)$$

which is tantamount to a condition

$$\text{div}\mathbf{A}(\mathbf{x},t) = 0. \quad (39)$$

It is convenient to set the vector potential for automatic fulfillment of conditions (38) and (39) in the following form

$$\begin{aligned}\mathbf{A}(\mathbf{x},t) &= LB_m\text{curl}\left(\psi_1(\mathbf{x},t)\nabla\psi_2(\mathbf{x})\right)\\ &= LB_m\left[\nabla\psi_1(\mathbf{x},t)\times\nabla\psi_2(\mathbf{x})\right],\end{aligned} \quad (40)$$

where L is the model parameter which has the dimension of length, and B_m is the model parameter that has the dimension of the magnetic field. (40) suggests that the vector potential is determined by its Eulerian potentials, namely by the time-dependent first potential $\psi_1(\mathbf{x},t)$ and the steady second potential $\psi_2(\mathbf{x})$ which should be independent of each other, i.e., their gradients should not be parallel. (40) and (37) imply the following expressions for the fields expressed through the functions $\psi_1(\mathbf{x},t)$ and $\psi_2(\mathbf{x})$:

$$\left.\begin{aligned}&\mathbf{B}(\mathbf{x},t) = B_{x0}\mathbf{e}_x + B_{y0}\mathbf{e}_y + \text{curl}\mathbf{A}(\mathbf{x},t)\\ &= B_{x0}\mathbf{e}_x + B_{y0}\mathbf{e}_y\\ &+ LB_m\text{curlcurl}\left(\psi_1(\mathbf{x},t)\nabla\psi_2(\mathbf{x})\right),\\ &\mathbf{E}(\mathbf{x},t) = -\frac{\partial\mathbf{A}(\mathbf{x},t)}{\partial t}\\ &= LB_m\left[\nabla\psi_2(\mathbf{x})\times\nabla\frac{\partial\psi_1(\mathbf{x},t)}{\partial t}\right].\end{aligned}\right\} \quad (41)$$

We assume that the SMI starts to oscillate at the time T_0 with the period Θ. It is convenient to present time in the following form: $t = T_0 + n_t\Theta + \tau$, where τ is the current phase of island oscillations, and $n_t = [(t-T_0)/\Theta] \in \mathbb{Z}$ is an integer. The parametrization of an ellipsoid with semiaxes oscillating around their mean values L_x, L_y, L_z with a period $\Theta = 2\pi/\omega$ can be chosen as the first potential $\psi_1(\mathbf{x},t)$:

$$\left.\begin{aligned}&\psi_1(\mathbf{x},t)\\ &= \exp\left(-|S_x(x,\tau)|^2 - |S_y(y,\tau)|^2 - |S_z(z,\tau)|^2\right),\\ &\text{where}\\ &S_x(x,\tau) = \frac{x-x_0}{L_x - \lambda_x\sin\omega\tau},\\ &S_y(y,\tau) = \frac{y-y_0}{L_y - \lambda_y\sin\omega\tau},\\ &S_z(z,\tau) = \frac{z-z_0}{L_z - \lambda_z\sin\omega\tau}.\end{aligned}\right\} \quad (42)$$

Here, $\mathbf{x}_0 = (x_0, y_0, z_0)$ is the coordinates of the center of the SMI, $\lambda_x, \lambda_y, \lambda_z$ is the amplitude of oscillations of the semiaxes, which must satisfy the condition $0 < \lambda_k < L_k/2$, $k = x, y, z$.

It is possible to choose the following function as the second potential:

$$\psi_2(\mathbf{x}) = \frac{1}{2}(\mathbf{x}-\mathbf{x}_0)^2, \text{ i.e. } \nabla\psi_2(\mathbf{x}) = \mathbf{x}-\mathbf{x}_0. \quad (43)$$

We have examined osicllations of a SMI of the three possible spatial sizes $L = L_x$: $L = 10^8$; 1.5×10^8; 2×10^8 m, in our calculations of the energy obtained by particles. The remaining spatial model parameters were determined as follows: $L_y = L_z = L/2$, $\lambda_x = \lambda_z = 0$, $\lambda_y = L_y/2 = L/4$. An island in the form of an ellipsoid elongated in the X direction was considered in which only the semiaxis in the Y direction oscillates. The components of the magnetic field of the solar wind had the values of $B_{x0} = B_{y0} = 5$ nT. Three variants were considered for the amplitude of oscillations of the magnetic field of

the SMI: $B_m = 0.5B_{x0}$; $0.75B_{x0}$; B_{x0}, as well as two variants of the oscillation period $\Theta = 2\pi/\omega = 300$; 600 s.

The origin of the frame of reference K' can be conveniently placed in the center of the island, therefore $x_0 = 0$. It is also reasonable to introduce dimensionless variables $\tilde{x} = x/L$, $\tilde{y} = y/L$, $\tilde{z} = z/L$ and the parameter $\tilde{\lambda} = \lambda_y/L = 1/4$.

The following expressions for the electric and magnetic field components can be obtained from formulas (3), (41)–(43):

$$\begin{aligned}\psi_0(t) &= \left(1 - 2\tilde{\lambda}\sin\omega\tau\right)^{-2},\\ \psi_1(\mathbf{x},t) &= \exp\left(-\tilde{x}^2 - 4\tilde{z}^2 - 4\tilde{y}^2\psi_0(t)\right),\end{aligned} \tag{44}$$

$$\left.\begin{aligned}B_x(\mathbf{x},t) &= B_{x0} + 4B_m\psi_1(\mathbf{x},t)\\ &\times \tilde{x}\left(1 - 12\tilde{z}^2 + 2\psi_0(t)\left(1 + 2\tilde{y}^2\left(1 - 4\psi_0(t)\right)\right)\right),\\ B_y(\mathbf{x},t) &= B_{y0} + 2B_m\psi_1(\mathbf{x},t)\\ &\times \tilde{y}\left(5 - 2\tilde{x}^2 - 32\tilde{z}^2 + 8\psi_0(t)\left(4\tilde{z}^2 + \tilde{x}^2 - 1\right)\right),\\ B_z(\mathbf{x},t) &= 2B_m\psi_1(\mathbf{x},t)\,\tilde{z}\left(6\tilde{x}^2 - 7 + 4\psi_0(t)\right.\\ &\times \left.\left(1 - 32\tilde{\lambda}\tilde{y}^2\psi_0(t)\left(1 - \tilde{\lambda}\sin\omega\tau\right)\sin\omega\tau\right)\right)\end{aligned}\right\} \tag{45}$$

$$E_0(\mathbf{x},t) = \frac{32\omega L B_m\tilde{\lambda}\tilde{y}\cos\omega\tau}{\left(1 - 2\tilde{\lambda}\sin\omega\tau\right)^3}\psi_1(\mathbf{x},t), \tag{46}$$

$$\left.\begin{aligned}E_x(\mathbf{x},t) &= E_0(\mathbf{x},t)\\ &\times \tilde{z}\left(1 - 32\tilde{\lambda}\tilde{y}^2\psi_0(t)\left(1 - \tilde{\lambda}\sin\omega\tau\right)\sin\omega\tau\right),\\ E_y(\mathbf{x},t) &= -3E_0(\mathbf{x},t)\,\tilde{x}\tilde{z}\tilde{y},\\ E_z(\mathbf{x},t) &= E_0(\mathbf{x},t)\,\tilde{x}\left(\tilde{y}^2\left(4\psi_0(t) - 1\right) - 1\right).\end{aligned}\right\} \tag{47}$$

Note that (45)–(47) suggest the existence of the significant longitudinal electric field in the main region of the elliptic SMI for the practically entire oscillation period

$$\left\{\mathbf{x}: \left(x^2 + 4y^2 + 4z^2\right)/L^2 \le 1\right\}$$

MODELING TECHNIQUE

It is necessary to solve the Cauchy problem numerically for the system of equations of the charge motion in the electromagnetic field (so-called Newton–Lorentz system) to calculate the trajectory of a particle with the charge e and the rest mass m_0. It has the following form in the SI system in the relativistic case:

$$\begin{aligned}\frac{d\mathbf{x}(t)}{dt} &= \mathbf{v}(t), \quad \mathbf{p}(\mathbf{v}) = \frac{m_0\mathbf{v}}{\sqrt{1 - |\mathbf{v}|^2/c^2}},\\ \frac{d\mathbf{p}(\mathbf{v}(t))}{dt} &= e\left(\mathbf{E}(\mathbf{x}(t),t) + [\mathbf{v}(t)\times\mathbf{B}(\mathbf{x}(t),t)]\right),\end{aligned} \tag{48}$$

where c is the speed of light in vacuum, and $\mathbf{p}$ is the momentum. This system in the classical limit $|\mathbf{v}|/c \ll 1$ takes the following form

$$\begin{aligned}\frac{d\mathbf{x}(t)}{dt} &= \mathbf{v}(t),\\ \frac{d\mathbf{v}(t)}{dt} &= \frac{e}{m_0}\left(\mathbf{E}(\mathbf{x}(t),t) + [\mathbf{v}(t)\times\mathbf{B}(\mathbf{x}(t),t)]\right).\end{aligned} \tag{49}$$

The initial conditions are as follows:

$$\mathbf{x}\left(t^0\right) = \mathbf{x}^0, \quad \mathbf{v}\left(t^0\right) = \mathbf{v}^0. \tag{50}$$

The kinetic energy in electron-volts $W(v)$ is tied to the velocity modulus $v = |\mathbf{v}|$ by the following expressions:

$$\begin{aligned}W(|\mathbf{v}|) &= \frac{m_0c^2}{e}\left(\frac{1}{\sqrt{1 - |\mathbf{v}|^2/c^2}} - 1\right),\\ \frac{|\mathbf{v}|}{c} &= \sqrt{\frac{eW}{m_0c^2}\left(\frac{eW}{m_0c^2} + 2\right)}\Bigg/\left(\frac{eW}{m_0c^2} + 1\right).\end{aligned} \tag{51}$$

In the classical limit, it transforms into the kinetic energy for the classical approximation: $W(v) \to \frac{1}{2e}m_0v^2$ for $\frac{v}{c} \to 0$. Note that Eqs. (48) and (51) imply the following equation

$$\frac{dW(|\mathbf{v}(t)|)}{dt} = \left(\mathbf{E}(\mathbf{x}(t),t), \mathbf{v}(t)\right). \tag{52}$$

To save computational resources during simulations of the particle trajectory, we employ the time step within the classical system of equations (49) if the parameter $\beta = |\mathbf{v}|/c < \beta_0 = 0.02$ (which corresponds to the kinetic energy of $W_0 \approx 188$ keV) during the calculation of the trajectory, the time step within classical system of equations (49) is used to save computational resources; and if $\beta \ge \beta_0 = 0.02$, the time step is in the relativistic system of equations (48). The numerical method for the proton trajectory calculations within the classical and the relativistic system of equations is given in detail in APPENDIX.

It is convenient to denote the solution of Cauchy problem (48), (50) for the subsequent presentation as

$$\mathbf{x}(t) = \mathbf{X}\left(t,t^0,\mathbf{x}^0,\mathbf{v}^0\right), \quad \mathbf{v}(t) = \mathbf{V}\left(t,t^0,\mathbf{x}^0,\mathbf{v}^0\right), \tag{53}$$

where t^0,$\mathbf{x}^0$, and $\mathbf{v}^0$ are the initial time, the initial point, and the initial velocity, respectively, for the analysis of the dependence of the modeling results on the initial particle data. The superscript zero denotes the initial data here and elsewhere. These vector func-

tions satisfy the following equations and initial conditions:

$$\frac{\partial \mathbf{X}\left(t,t^0,\mathbf{x}^0,\mathbf{v}^0\right)}{\partial t} = \mathbf{V}\left(t,t^0,\mathbf{x}^0,\mathbf{v}^0\right), \quad \frac{\partial \mathbf{V}\left(t,t^0,\mathbf{x}^0,\mathbf{v}^0\right)}{\partial t} = e'\left(\mathbf{E}\left(\mathbf{X}\left(t,t^0,\mathbf{x}^0,\mathbf{v}^0\right),t\right) + \left[\mathbf{V}\left(t,t^0,\mathbf{x}^0,\mathbf{v}^0\right)\times \mathbf{B}\left(\mathbf{X}\left(t,t^0,\mathbf{x}^0,\mathbf{v}^0\right),t\right)\right]\right),$$
$$\mathbf{X}\left(t^0,t^0,\mathbf{x}^0,\mathbf{v}^0\right) = \mathbf{x}^0, \quad \mathbf{V}\left(t^0,t^0,\mathbf{x}^0,\mathbf{v}^0\right) = \mathbf{v}^0.$$

Note that the electromagnetic field of the SMI additional to the electromagnetic field in the solar wind gradually increases from zero to the maximum value at SMI edges, and the flux of pre-accelerated protons coming from the HCS ripple can be injected into any part of the SMI. This happens any time, at different phases of oscillations of the SMI. Therefore, the following approach can be used to model possible acceleration of protons. A rather wide set of starting points $\left\{\mathbf{x}^0\left[k_x\right]\right\}$ inside the elliptic SMI is chosen:

$$\Omega_0 = \left\{\mathbf{x}: \left(x^2 + 4y^2 + 4z^2\right)\Big/ L^2 \le 1\right\}. \tag{54}$$

We also set of initial phases of oscillations of the island $\tau^0\left[k_t\right]$ from 0 to Θ with the step $\frac{\Theta}{16}$ which corresponds to the set of initial times $\left\{t^0\left[k_t\right] = T_0 + \tau^0\left[k_t\right]\right\}$. For simplicity, time is counted from the beginning of oscillations of the SMI, i.e. we assume $T_0 = 0$ and identify the initial time and the initial phase: $t^0\left[k_t\right] = \tau^0\left[k_t\right]$.

The set of options for the initial velocity $\mathbf{v}^0$ is constructed as follows. The set of initial kinetic energies $W^0\left[k_w\right]$ in the range from 10 eV to 100 keV is chosen. The step is 10 eV in the range from 10 eV to 0.5 keV and 0.5 keV in the range from 0.5 to 100 keV. Each initial energy in eV corresponds to the initial velocity modulus determined by the second formula in (51):

$$v^0\left(W^0\right) = c\sqrt{\frac{eW^0}{m_0c^2}\left(\frac{eW^0}{m_0c^2}+2\right)}\Bigg/\left(\frac{eW^0}{m_0c^2}+1\right). \tag{55}$$

The set of $N_{(\alpha\beta)} = 2N_\alpha\left(N_\beta+1\right) = 360\times 181$ initial velocities with the given initial energy W^0 and with the step of 1 degree in the velocity direction angles can be introduced as

$$\left\{\mathbf{v}^0\left[W^0,k_\alpha,k_\beta\right],\ k_\alpha = -N_\alpha+1,\ldots,N_\alpha,\ k_\beta = 0,\ldots,N_\beta,\quad N_\alpha = N_\beta = 180\right\} \tag{56}$$

It is determined by the following formulas for the components of the initial velocity:

$$\left.\begin{aligned} v_x^0\left[W^0,k_\alpha,k_\beta\right] &= v^0\left(W^0\right)\sin\left(\pi k_\beta/N_\beta\right)\cos\left(\pi k_\alpha/N_\alpha\right),\\ v_y^0\left[W^0,k_\alpha,k_\beta\right] &= v^0\left(W^0\right)\sin\left(\pi k_\beta/N_\beta\right)\sin\left(\pi k_\alpha/N_\alpha\right),\\ v_z^0\left[W^0,k_\alpha,k_\beta\right] &= v^0\left(W^0\right)\cos\left(\pi k_\beta/N_\beta\right).\end{aligned}\right\} \tag{57}$$

Therefore, the set of initial conditions is formed $\left\{t^0\left[k_t\right],\mathbf{x}^0\left[k_x\right],\mathbf{v}^0\left[W^0\left[k_w\right],k_\alpha,k_\beta\right]\right\}$. We employ here the frame of reference K' moving along with the solar wind in which the island center is steady and the magnetic and electric fields are determined by (44)–(47), which is described in the "System Geometry" section. The trajectory control region (the modeling region) is defined as the rectangular parallelepiped

$$\Pi = \left\{\mathbf{x}: |x/L| \le 1.25,\ |y/L| \le 1,\ |z/L| \le 0.75\right\}, \tag{58}$$

containing the ellipsoid Ω_0, defined according to (4.7).

The proton trajectories are calculated for each chosen $\mathbf{F}^{(i)}\left[k_f\right](\mathbf{x},t)$ of the SMI (where $\mathbf{F}^{(i)} = \left\{\mathbf{B}^{(i)},\mathbf{E}^{(i)}\right\}$) described in the previous section; and for each initial condition $\left(t^0,\mathbf{x}^0,\mathbf{v}^0\right)$ Cauchy problem (47), (50) is solved until the particle escape from the control region Π. As a result, we calculate time for which the trajectory remains within the control region Π, which we denote by $T_{\text{end}}\left(t^0,\mathbf{x}^0,\mathbf{v}^0\right)$, the escape point coordinate $\mathbf{x}_{\text{end}}\left(t^0,\mathbf{x}^0,\mathbf{v}^0\right)$, and the escape velocity $\mathbf{v}_{\text{end}}\left(t^0,\mathbf{x}^0,\mathbf{v}^0\right)$. The latter gives the following escape energy (in eV) according to the first formula in (51):

$$W_{\text{end}}\left(t^0,\mathbf{x}^0,\mathbf{v}^0\right) = \frac{m_0c^2}{e}\left(\frac{1}{\sqrt{1-\left|\mathbf{v}_{\text{end}}\left(t^0,\mathbf{x}^0,\mathbf{v}^0\right)\right/c|^2}}-1\right). \tag{59}$$

For the initial time t^0, the starting point $\mathbf{x}^0$, and set (57) of initial velocities with a given initial energy W^0, we analyze below the average energy of particles

$\langle W_{\text{end}}\rangle\left(t^0,\mathbf{x}^0,W^0\right)$ and the average time $\langle T_{\text{end}}\rangle\left(t^0,\mathbf{x}^0,W^0\right)$ that particles spend in the control region Π treating the parameters as the most indicative. Their values can be determined through the parameters of each trajectory as follows:

$$\langle W_{\text{end}}\rangle\left(t^0,\mathbf{x}^0,W^0\right) = \frac{1}{N_{(\alpha\beta)}}\sum_{k_\beta=0}^{N_\beta}\sum_{k_\alpha=-N_\alpha+1}^{N_\alpha} W_{\text{end}}\left(t^0,\mathbf{x}^0,\mathbf{v}^0\left[W^0,k_\alpha,k_\beta\right]\right), \quad (60)$$

$$\langle T_{\text{end}}\rangle\left(t^0,\mathbf{x}^0,W^0\right) = \frac{1}{N_{(\alpha\beta)}}\sum_{k_\beta=0}^{N_\beta}\sum_{k_\alpha=-N_\alpha+1}^{N_\alpha} T_{\text{end}}\left(t^0,\mathbf{x}^0,\mathbf{v}^0\left[W^0,k_\alpha,k_\beta\right]\right). \quad (61)$$

For each initial set of initial times and coordinates $\left(t^0,\mathbf{x}^0\right)$, the quantities used in (60) and (61) are functions of one variable, which is the initial energy $W^0[k_w]$. The graphs of these functions clearly demonstrate the presence of acceleration.

The anisotropy of protons emitted from the control region Π is also of interest. For a given set $\left(t^0,\mathbf{x}^0,W^0\right)$, it can be described using the distribution function $f\left[t^0,\mathbf{x}^0,W^0\right](\alpha,\beta)$ of the direction of the escape velocities $\mathbf{v}_{\text{end}}\left(t^0,\mathbf{x}^0,\mathbf{v}^0\left[W^0,k_\alpha^0,k_\beta^0\right]\right)$ over the escape angles in the spherical coordinate system $\alpha\in(-\pi;\pi]$ and $\beta\in[0;\pi]$. These angles are determined by the following formulas

$$\left.\begin{aligned}\beta\left[t^0,\mathbf{x}^0,W^0\right]\left(k_\alpha^0,k_\beta^0\right) &= \arccos\left(v_{\text{end},z}\left(t^0,\mathbf{x}^0,\mathbf{v}^0\left[W^0,k_\alpha^0,k_\beta^0\right]\right)\Big/\left|\mathbf{v}_{\text{end}}\left(t^0,\mathbf{x}^0,\mathbf{v}^0\left[W^0,k_\alpha^0,k_\beta^0\right]\right)\right|\right),\\ \alpha\left[t^0,\mathbf{x}^0,W^0\right]\left(k_\alpha^0,k_\beta^0\right) &= 2\arctan\left(\frac{v_{\text{end},y}\left(t^0,\mathbf{x}^0,\mathbf{v}^0\left[W^0,k_\alpha^0,k_\beta^0\right]\right)}{\left|\mathbf{v}_{\text{end}}\left(t^0,\mathbf{x}^0,\mathbf{v}^0\left[W^0,k_\alpha^0,k_\beta^0\right]\right)\right|+v_{\text{end,x}}\left(t^0,\mathbf{x}^0,\mathbf{v}^0\left[W^0,k_\alpha^0,k_\beta^0\right]\right)}\right),\end{aligned}\right\} \quad (62)$$

which are equivalent to ratios

$$v_{\text{end},x} = |\mathbf{v}_{\text{end}}|\sin\beta\cos\alpha,\ \ v_{\text{end},y} = |\mathbf{v}_{\text{end}}|\sin\beta\sin\alpha,$$
$$v_{\text{end},z} = |\mathbf{v}_{\text{end}}|\cos\beta.$$

Values of the function $f\left[t^0,\mathbf{x}^0,W^0\right](\alpha,\beta)$ in grid nodes

$$\beta[k_\beta] = \pi k_\beta/N_\beta,\ \ \alpha[k_\alpha] = \pi k_\alpha/N_\alpha,$$
$$k_\alpha = -N_\alpha+1,\ldots,N_\alpha,\ \ k_\beta = 0,\ldots,N_\beta,$$
$$N_\alpha = N_\beta = 180$$

are determined by the linear weighting according to the following formulas

$$f\left[t^0,\mathbf{x}^0,W^0\right](\alpha[k_\alpha],\beta[k_\beta]) = \sum_{k_\beta^0=0}^{N_\beta}\sum_{k_\alpha^0=-N_\alpha+1}^{N_\alpha} W_1\left(\frac{\alpha[k_\alpha]-\alpha\left[t^0,\mathbf{x}^0,W^0\right]\left(k_\alpha^0,k_\beta^0\right)}{\Delta\alpha}\right) \times W_1\left(\frac{\beta[k_\beta]-\beta\left[t^0,\mathbf{x}^0,W^0\right]\left(k_\alpha^0,k_\beta^0\right)}{\Delta\beta}\right), \quad (63)$$

where $\Delta\alpha = \pi/N_\alpha$, $\Delta\beta = \pi/N_\beta$ and $W_1(\lambda) = \max(1-|\lambda|,0)$.

RESULTS OF THE MODELING

We will discuss below the results of modeling of particle acceleration in a SMI with the size of $L = 10^8$ m, the period of oscillation of $\Theta = 600$ s, and the amplitude of oscillations of the magnetic field of $B_m = 0.75B_{x0} = 3.75$ nT. Figure 4 shows the average energies of the particles that escape from the plasmoid, depending on their initial energies W^0 in keV plotted along the X axis. Curves *1–6* in the three panels of Figure 4 correspond to six different starting points inside the SMI. One can see that there are points of effective particle acceleration inside the island (see curves *1–3)*, and the points of weak or absent acceleration (curves *4–6*). The region $\Omega(t^0)$ characterizes the neighborhood of the starting point $\mathbf{x}^0/L = (0.5;0.2;0.25)$. The set of initial data $\left[t_1^0;t_2^0\right]\times\Omega\left(t^0\right)\subset\mathbb{R}^4_{t,\mathbf{x}}$ in their entirety represents the "acceleration" set of points. Particles injected into acceleration points gain substantial energy compared with initial. The average escape energy of such particles is $\langle W_{\text{end}}\rangle\left(t^0,\mathbf{x}^0,W^0\right) > 150$ keV in the whole considered range of initial energies. At the same time, the phase $t^0 = \Theta/4$ is central in the interval of the "accelerating" initial phases $\left[t_1^0;t_2^0\right]\approx[\Theta/8;3\Theta/8]$. There is either no acceleration outside the "accelerating" set of starting points $\left(t^0,\mathbf{x}^0\right)\notin\left[t_1^0;t_2^0\right]\times\Omega(t^0)$ or it is weak and occurs in a limited range of low initial energies only. The acceleration region $\Omega(t^0)$ can change size in time, i.e., it is maximal at $t^0 = \Theta/4$ and grows smaller at other t^0. In Fig. 4, curve *1* corresponds to the center of the acceleration region. The shape of the curve shows that the average escape energy of accelerated

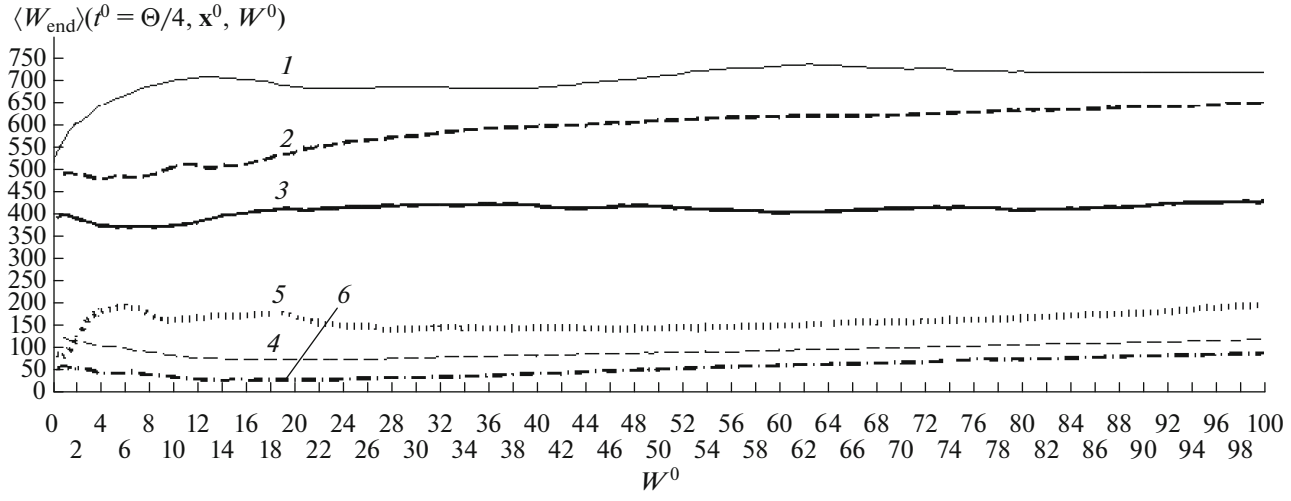

Fig. 4. Average escape energy $\langle W_{\text{end}}\rangle\left(t^0, \mathbf{x}^0, W^0\right)$ in keV for several starting points in the SMI with the size $L = 10^8$ m, the magnetic field $B_m = 0.75B_{x0} = 3.75$ nT, the oscillation period $\Theta = 600$ s, and the initial time $t^0 = \Theta/4$. The initial energies of particles W^0 in keV are plotted on the abscissa. Curves *1–3* correspond to the starting points $\mathbf{x}^0/L = (0.5;0.2;0.25)$; $\mathbf{x}^0/L = (0.4;0.16;0.2)$ and $\mathbf{x}^0/L = (0.6;0.24;0.3)$ in the acceleration region. Curves *4–6* correspond to the starting points $\mathbf{x}^0/L = (0.2;0.1;0.1)$, $\mathbf{x}^0/L = (0.7;0.28;0.35)$ and $\mathbf{x}^0/L = (-0.2;-0.1;-0.1)$.

particles for the initial energies $W^0 \geq 10$ keV exceeds 700 keV and depends weakly on the initial energy W^0 of particles injected into the SMI. Curves *2* and *3* correspond to the central part of the acceleration region $\Omega\left(t^0 = \Theta/4\right)$. One can see that the average escape energy of particles injected into these regions exceeds 600 keV (curve *2*) and 400 keV (curve *3*), respectively, and also depends on initial energies W^0 very weakly. It turns out that particles of very different energies (differing by times and even orders of magnitude) originating from the same starting point leave the control region with close final energies.

Let us examine below the points lying outside the acceleration region $\mathbf{\Omega}\left(t^0 = \Theta/4\right)$. Curve *5* shows the dependence of the escape energy of particles that leave the SMI close to the boundary of the acceleration region from the starting point $\mathbf{x}^0/L = (0.7;0.28;0.35)$. The average escape energies for such points exceed 150 keV and weakly depend on the initial energy, analogous to the case of particles injected into the acceleration region. Curves *4* and *6* are shown for particles with small energies of $W^0 \leq 10$ keV injected into the two selected starting points $\mathbf{x}^0/L = (0.2;0.1;0.1)$ and $\mathbf{x}^0/L = (-0.2;-0.1;-0.1)$. Such particles are accelerated to average energies of about 100 and 50 keV, respectively. There is almost no acceleration at higher initial energies W^0.

Figure 5 shows the average time in minutes $\langle T_{\text{end}}\rangle\left(t^0 = \Theta/4, \mathbf{x}^0, W^0\right)$ of the presence of the trajectory in the modeling region for the same trajectories as shown in Figure 4. An analysis of the behavior of curves *1*, *2*, and *3* shows that for the dependence of $\langle T_{\text{end}}\rangle\left(t^0 = \Theta/4, \mathbf{x}^0, W^0\right)$ on the initial energy W^0 in the range $W^0 \geq 20$ keV is also very weak for the trajectories from the inner part of the acceleration region $\Omega\left(t^0 = \Theta/4\right)$, and the average time of the trajectory occurrence in the control region is less than 2.7 min. At the same time, curve *6* shows that particles remain in the modeling region for quite a long time, from 8 to 13 min. Curves *4* and *5* show that the main differences in the times that particles spend in the system are observed mainly at low initial energies (less than 20 keV). The corresponding curves reach approximately the same values of the gained energy as for large initial energies.

If one compares different scenarios of SMI oscillations, the pattern is as follows: as the longitudinal inductive electric field increases, the interval of the initial phases at which particles gain energy above 150 keV becomes noticeably wider. Figure 6 shows results of modeling of particle acceleration in the SMI with the characteristic scale of $L = 1.5\times10^8$ m, the magnetic field $B_m = 3.75$ nT, and the period of oscilla-

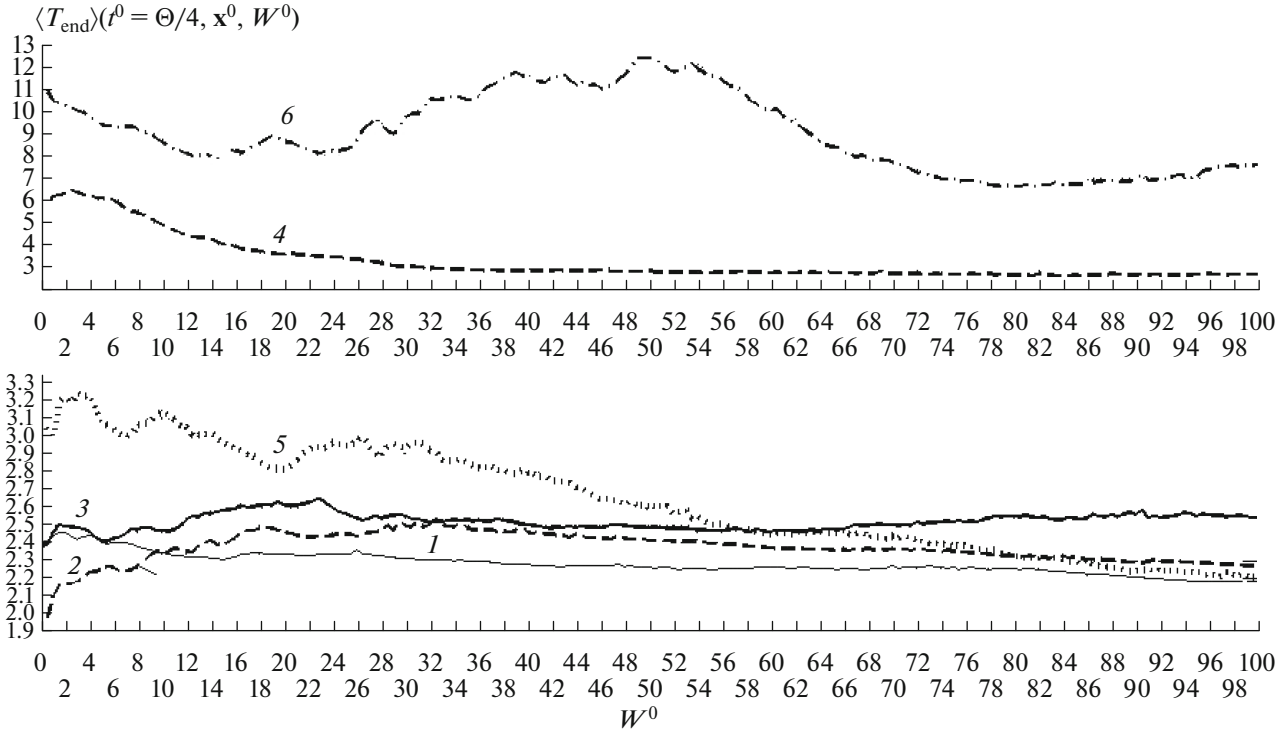

Fig. 5. Average time $\langle T_{\text{end}}\rangle\left(t^0, \mathbf{x}^0, W^0\right)$ in minutes during which the trajectory remains in the control region Π for several starting points for the scenario with $L = 10^8$ m, $B_m = 0.75B_{x0} = 3.75$ nT, the oscillation period Θ = 600 s, and the initial time $t^0 = \Theta/4$. Notations for the curves are the same as in Fig. 4.

tion Θ = 300 s. The amplitude of the electric field is three times larger compared with the first scenario presented in Figure 4, and the time interval of the acceleration region becomes $\left[t_1^0; t_2^0\right] \approx \left[\Theta/16; \Theta 7/16\right]$. The center of the acceleration region remains the same in spatial coordinates, but the region itself expands, and the average escape energy of particles increases several times in comparison with the previous case. Curve *1* in Figure 6 corresponds to the starting point $\mathbf{x}^0/L = (0.5; 0.2; 0.25)$, i.e., to the center of the acceleration region in which the average escape energy is maximum and exceeds 2 MeV being approximately three times higher than for the first configuration shown in Figure 4. Curve *2* corresponds to the acceleration region (similar to curve *3* in Fig. 4). The average energy of the particles escaping from this region increases about four times in comparison with the previous case. Curve *3* with the starting point $\mathbf{x}^0/L = (0.4; 0.16; 0.2)$ (similar to curve *2* in Fig. 4) shows ~2.3 times increase in the average escape energy. Curves *4–8* taken outside the accelerating region of the SMI show a general increase in the energy gain of the particles 2–4 times larger compared with the configuration modeled in Fig. 4. Note that in this case particles are significantly accelerated even at the points where there is no acceleration at all or it is very weak in the configuration examined in Fig. 4.

Figure 7 shows the average time $\langle T_{\text{end}}\rangle\left(t^0 = \Theta/4, \mathbf{x}^0, W^0\right)$ in minutes during which the trajectory is in the modeling region starting from the same points as in Figure 6. A comparison of Figure 7 with Figure 5 shows that the average time spent by the trajectory in the control region $\Omega\left(t^0 = \Theta/4\right)$ is ~1.6 times smaller for the starting points from the central part of the acceleration region Π, which indicates stronger proton acceleration compared with the configuration modeled in Fig. 4.

We analyze below acceleration processes occurring at the same starting point inside the SMI in dependence on the phases (starting points in time) of the particles at the start of their motion in the system representing a SMI that oscillates with the period Θ = 300 s (the remaining parameters are indicated in the caption for Fig. 6). Figure 8 shows the average escape energies $\langle W_{\text{end}}\rangle\left(t^0, \mathbf{x}^0, W^0\right)$ for different initial times in the center of the acceleration region Ω. The particles are slightly accelerated in the range of initial energies $W^0 \le 65$ keV at the time $t^0 = 0$ (curve *1*). Sig-

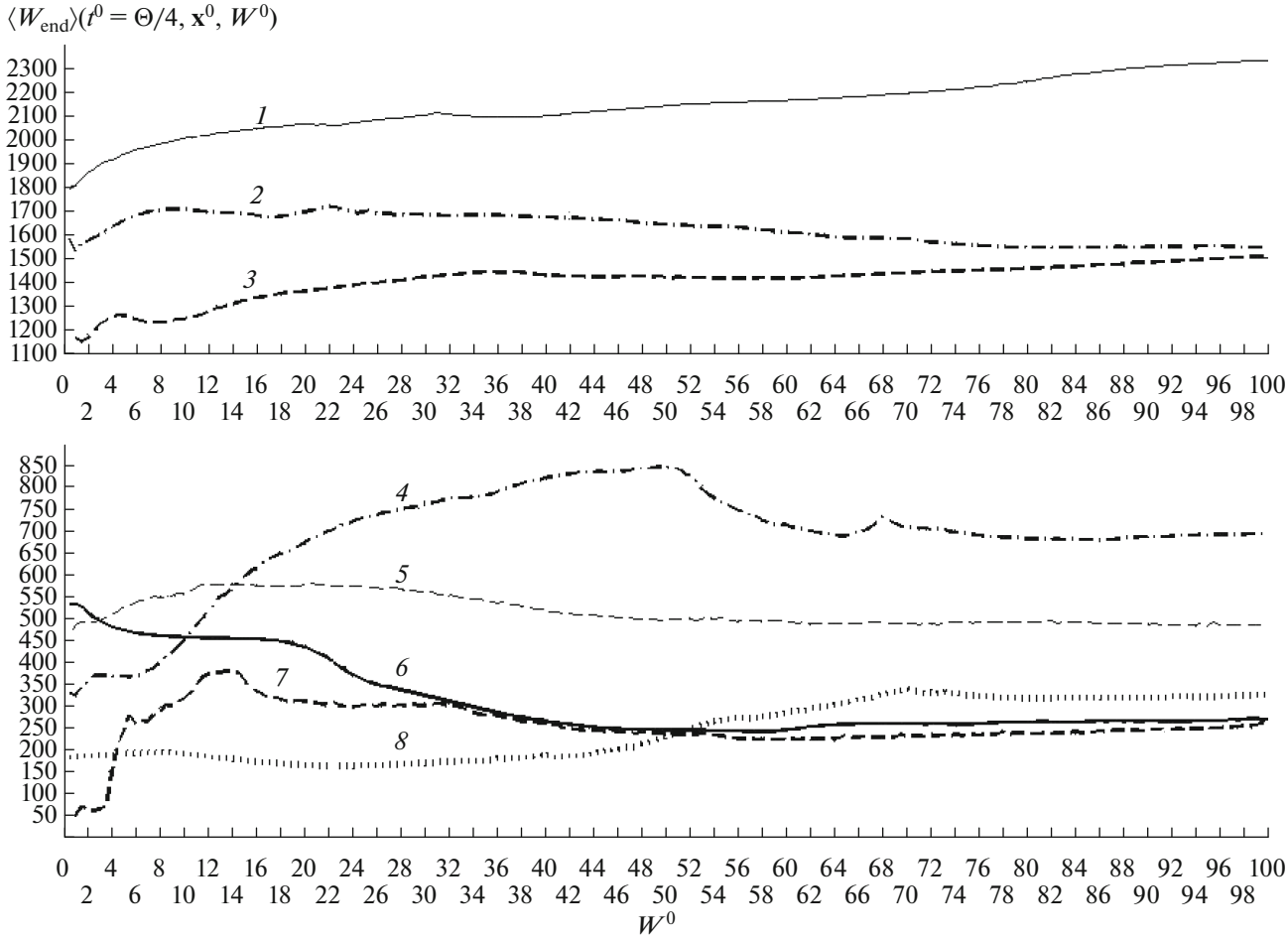

Fig. 6. Average escape energy $\langle W_{\text{end}} \rangle \left(t^0, \mathbf{x}^0, W^0 \right)$ (in keV) obtained by particles injected into several starting points as calculated for the SMI with the following parameters: $L = 1.5 \times 10^8$ m, $B_m = 3.75$ nT, $\Theta = 300$ s, and $t^0 = \Theta/4$. Curve *1* corresponds to the center of the acceleration region, the starting point $\mathbf{x}^0/L = (0.5;0.2;0.25)$, curve *2* corresponds to the starting point $\mathbf{x}^0/L = (0.6;0.24;0.3)$; curve *3*, $\mathbf{x}^0/L = (0.4;0.16;0.2)$; curve *4*, $\mathbf{x}^0/L = (0.7;0.28;0.35)$; curve *5*, $\mathbf{x}^0/L = (0.2;0.1;0.1)$; curve *6*, $\mathbf{x}^0/L = -(0.5;0.2;0.25)$, which is symmetrical to the center of the acceleration region; curve *7*; $\mathbf{x}^0/L = (0;0;0)$ at the center of the island, and curve *8*, $\mathbf{x}^0/L = (0.7;0.3;0.4)$.

nificant acceleration is detected at small initial energies $W^0 \le 20$ keV at $t^0 = \Theta/16$ (curve *2*) and particles are accelerated weaker in the other initial energies. Curves *3* and *7* show effective acceleration up to 700–800 keV and higher. Particles obtain the highest energy increment at $t^0 = \Theta/4$ (curve *5*) and $t^0 = 3\Theta/16; 5\Theta/16$ (curves *4*, *6*). Curves *8–11* ($t^0 = 3\Theta/8, 7\Theta/16, \Theta/2, 3\Theta/4, 7\Theta/8$) again show relatively weak acceleration with some differences, especially for the initial energies lower than 50 keV.

Note that there is no acceleration or it is weak for other initial times $t^0 > \Theta/2$. It is also possible to distinguish a similar time interval when particle acceleration is most effective for the second half of the period of oscillations of the SMI $(\Theta/2; \Theta)$.

Therefore, the results of our modeling show that there is not only a spatial but also a time interval ($\left[t_1^0; t_2^0\right] \approx [\Theta/16; 7\Theta/16]$) in which the interaction of the inductive electric field of an oscillating SMI with plasma particles is very effective, i.e., this mechanism can play a significant role in additional energization of pre-accelerated protons in magnetically inhomogeneous medium near the HCS. In this regard, one can suggest the resonant nature of particle acceleration inside an oscillating SMI similar to the phenomenon of parametric resonance.

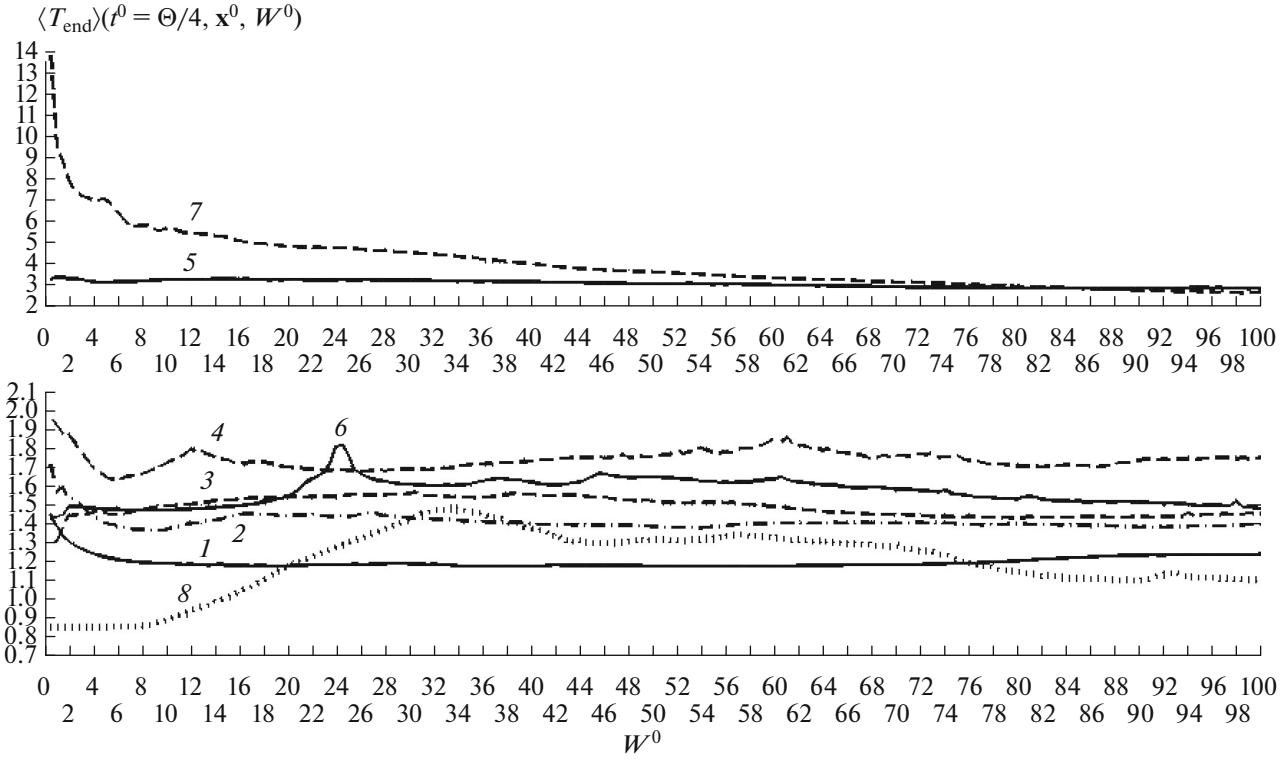

Fig. 7. Average time $\langle T_{\text{end}} \rangle \left(t^0, \mathbf{x}^0, W^0 \right)$ in minutes during which the trajectory remains in the control region Π for several starting points for the configuration with $L = 1.5 \times 10^8$ m, $B_m = 0.75 B_{x0} = 3.75$ nT, the oscillation period $\Theta = 300$ s, and the initial time $t^0 = \Theta/4$. Notations for the curves are the same as in Fig. 6.

At the next step, we will analyze the spatial distribution of the velocities of escaping particles. Figures 9 and 10 show plasma distribution functions depending on the velocity direction angles α, β (see (62), (63)) in the spherical coordinate system.

Figure 9 is given for the first modeled island that oscillates with the period of $\Theta = 600$ s. Figure 10 shows the results of the analysis for the second SMI configuration with $\Theta = 300$ s. A comparison of the two figures indicates the similarity of the overall structure of the distribution function regardless of the initial particle energies in the plasma. One can find that the flux of escaping particles has a clear spatial anisotropy showing maxima at certain azimuthal and latitudinal angles. A characterization of the direction of plasma escaping the SMI, in general, can be given as follows: particles leave the SMI with azimuthal angles of $60° \le \beta \le 120°$, concentrating around $\beta \sim 90°$. This means that the main particle escape zone is concentrated near the equatorial region of the magnetic bubble shown in Figure 2. On the other hand, the distribution of escaping particles is concentrated in the two symmetric regions with respect to the angle $\alpha \sim -30°$, namely at $\alpha \sim 60°$ and $\alpha \sim -120°$. This means that the particle escape is nonuniform and does not occur diffusely in all directions near the equator but is directed in the form of two beams occurring at 180° to each other. A comparison of Figures 9a and 9f shows that the pattern of distributions of escape directions becomes more and more complex with increasing particle energies. The boundaries of the picture of distributions become blurred, and it becomes complex in the velocity space.

The nature of the distribution function of escaping particles shown in Figure 10 for the case of the more rapidly oscillating SMI is similar to Figure 9. A comparison of Figures 9 and 10 shows that the distribution function $f\left[t^0, \mathbf{x}^0, W^0\right](\alpha, \beta)$ has a pronounced anisotropy for a given set of starting points $\left[t^0, \mathbf{x}^0, W^0\right]$. Since pre-accelerated particles that fall into an oscillating SMI possess energies from a rather limited range, one can expect that their acceleration also leads to formation of the anisotropic spatial distribution of velocities, similarly to one that can be obtained from the addition of different anisotropic distributions. Obviously, this nontrivial problem deserves a further detailed study.

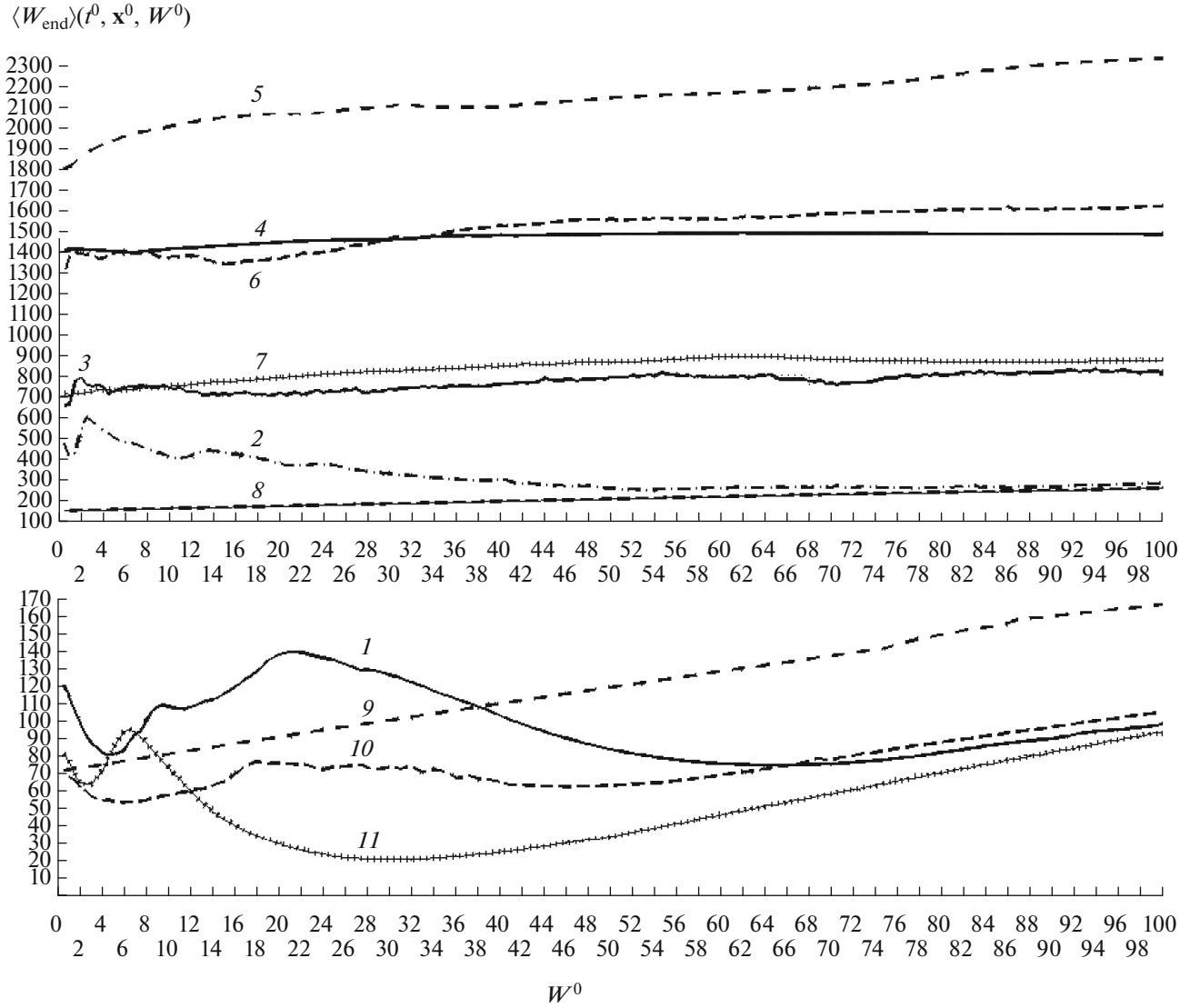

Fig. 8. Average escape energy $\langle W_{\text{end}}\rangle\left(t^0,\mathbf{x}^0,W^0\right)$ (keV) for different initial times t^0 for the variant with $L = 1.5\times10^8$ m, $B_m = 0.75B_{x0} = 3.75$ nT, the oscillation period of $\Theta = 300$ s for the starting point $\mathbf{x}^0/L = (0.5;0.2;0.25)$, the center of the acceleration region. Curves *1*–*11* correspond to the initial times: (*1*) $t^0 = 0$, (*2*, *3*) $t^0 = \Theta/16$, (*4*) $t^0 = \Theta/8$, (*5*) $t^0 = 3\Theta/16$, (*6*) $t^0 = 5\Theta/16$, (*7*) $t^0 = 3\Theta/8$, (*8*) $t^0 = 7\Theta/16$, (*9*) $t^0 = \Theta/2$, (*10*) $t^0 = 3\Theta/4$, and (*11*) $t^0 = 7\Theta/8$.

RESULTS AND DISCUSSION

The results of our study show that the examined system demonstrates the diverse and complex behavior similar to parametric resonance. The behavior of the system can change dramatically with small changes in both the scenario and the input parameters. The modeling results show that protons pre-accelerated in the HCS obtain further acceleration in an oscillating SMI if they are injected into the acceleration set of initial positions $\left(\tau^0,\mathbf{x}^0\right)\in\left[t_1^0;t_2^0\right]\times\Omega\left(\tau^0\right)$, where $\left[t_1^0;t_2^0\right]$ is the interval of initial phases in which pre-accelerated protons gain energy effectively, and $\Omega(\tau^0)$ is the acceleration region of the starting points. At the same time, pre-accelerated protons should fall into the region of the center $\mathbf{x}^{(c)}$ of the accelerating region of the starting points $\Omega(\tau^0)$ in order to achieve the maximum possible escape energy. Maximal acceleration occurs at time close to the oscillation phase in a quarter of the period, i.e., to the position $\left(\tau^0,\mathbf{x}^0\right)\approx\left(\frac{\Theta}{4},\mathbf{x}^{(c)}\right)$. As one can see in Figures 5 and 7, the average escape energy decreases several times and

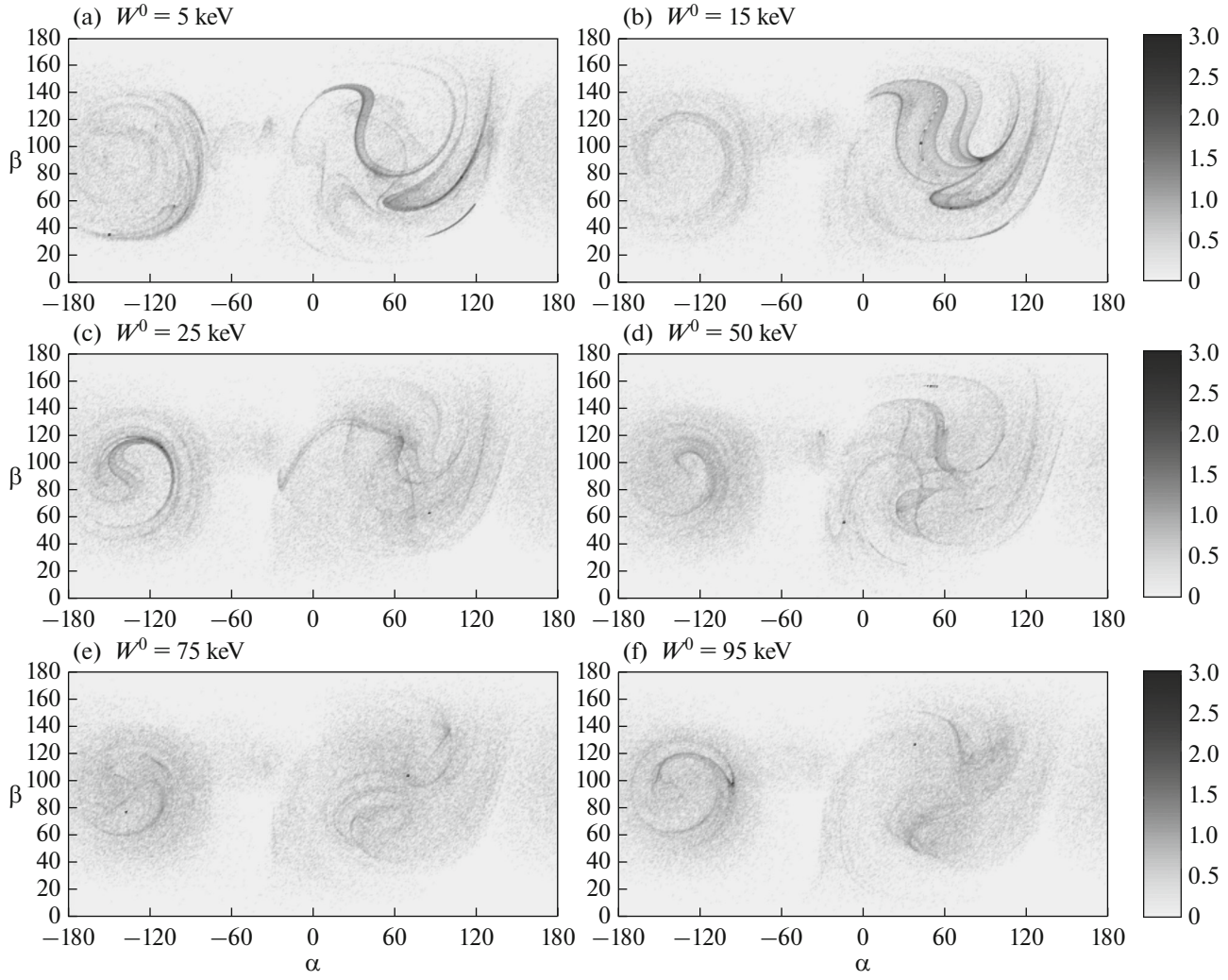

Fig. 9. Logarithm of the distribution function $\log\left(1+f\left[t^0,\mathbf{x}^0,W^0\right](\alpha,\beta)\right)$ (see the MODELING TECHNIQUE section) obtained for six initial energies W^0 depending on the directions of particle escape velocities for the slowly oscillating plasmoid (Θ = 600 s) corresponding to Fig. 4. The starting point $\mathbf{x}^0/L = (0.5;0.2;0.25)$ is selected at the center of the acceleration region. The initial time $t^0 = \Theta/4$. The distribution functions are shown for the following energies: (a) $W^0 = 5$, (b) $W^0 = 15$, (c) 25, (d) 50, (e) 75, and (f) 95 keV.

further by an order of magnitude as the deviation from the initial position in which the acceleration is most effective increases.

Our estimates based on the generalized Ohm's law show that the potential electric field of the order of $E_p \sim 10^{-6}$ V/m can appear in an oscillating SMI due to small charge separation (see the "System geometry..." section). The maximum values of the longitudinal inductive electric field turn out to be of the order of $E_{\|} \sim 10^{-4}$ V/m, and the spatial distribution of the maxima $E_{\|}$ is significantly nonuniform. The used inductive electric field taken at the upper boundary of possible values makes it possible to model the process of multiple interaction of particles with SMIs of the whole system via a single calculation of a single interaction of a pre-accelerated proton with one SMI. If the proton preaccelerated by magnetic reconnection at the HCS interacts with a SMI, it is scattered by inhomogeneities of the magnetic field and accelerated by the longitudinal electric field. Many of pre-accelerated protons can experience multiple (from 10 to 100) interactions with different islands of the system, as a result of which they can obtain significant acceleration to energies several orders of magnitude greater than initial, similarly to the collective acceleration process in SMIs described in (Zank et al., 2014; 2015a; 2015b;

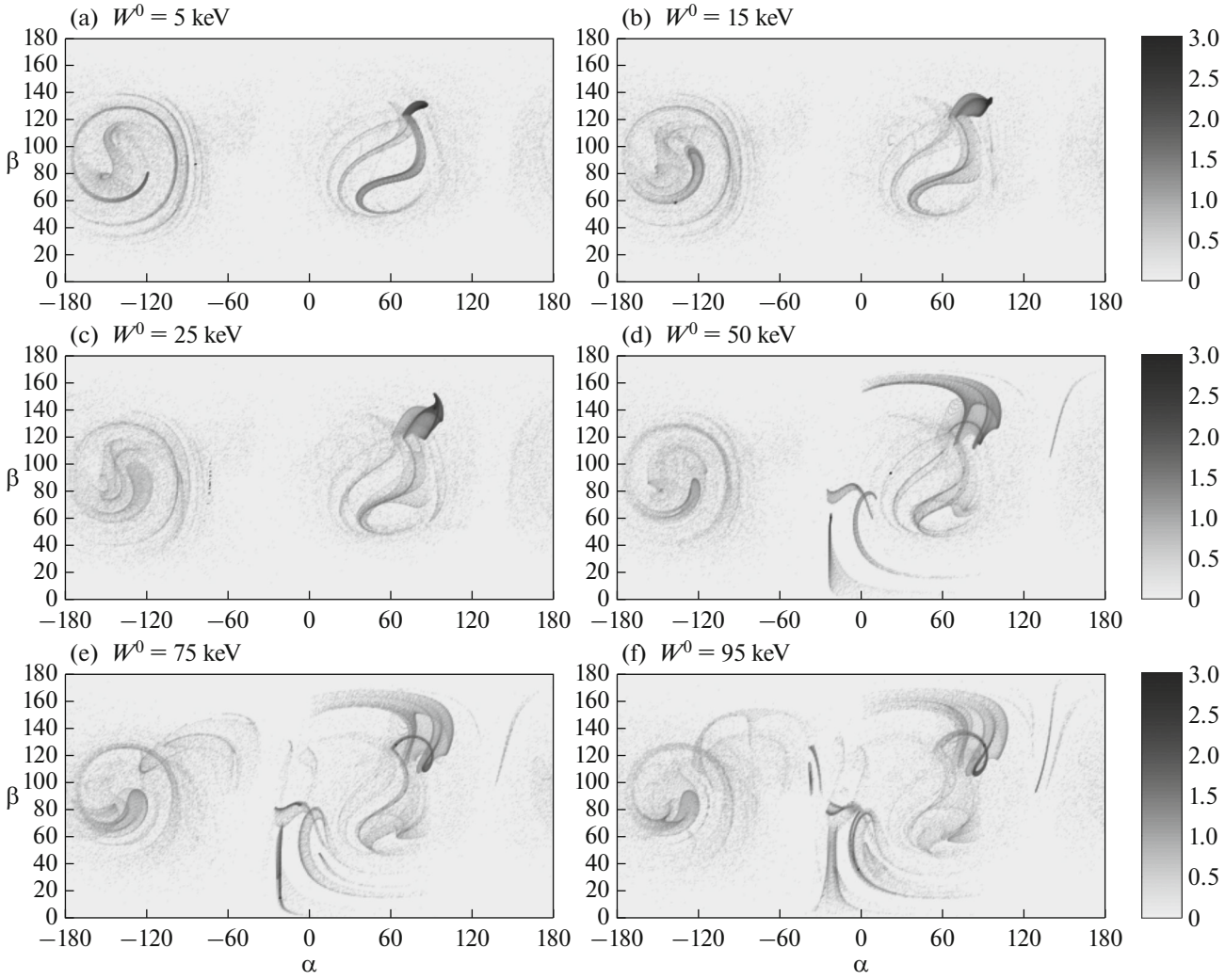

Fig. 10. Function $\log\left(1 + f\left[t^0, \mathbf{x}^0, W^0\right](\alpha,\beta)\right)$ of the distribution function $f\left[t^0, \mathbf{x}^0, W^0\right](\alpha,\beta)$ of the direction of escape velocities for escape angles calculated for the scenario with $L = 1.5\times10^8$ m, $B_m = 0.75B_{x0} = 3.75$ nT, the oscillation period of $\Theta = 300$ s for the starting point $\mathbf{x}^0/L = (0.5;0.2;0.25)$, i.e., the center of the acceleration region of the starting points, and the best for accelerating the initial time $t^0 = \Theta/4$ for six initial energies W^0. (a) $W^0 = 5$, (b) $W^0 = 15$, (c) $W^0 = 25$, (d) $W^0 = 50$, (e) $W^0 = 75$, and (f) $W^0 = 95$ keV.

Zhou et al., 2015; le Roux et al., 2015; 2016). This simplified approach makes it possible to identify the main qualitative features of the acceleration process by the longitudinal electric field in SMIs and to compare the results with spacecraft observations.

So far, it becomes clear that such behavior of the SMI system is in good agreement (at the qualitative and quantitative level) with in situ measurements of energetic protons locally accelerated to energies ranging from hundreds of keV to several MeV obtained during passages of spacecraft through SMIs near the HCS (Khabarova et al., 2015a; 2015b; 2016). The problem posed and solved in this paper is important because the considered situation does not require any additional sources of disturbances in addition to the surface waves at the HCS, which are observed in quiet conditions and have been well known for several decades (Musielak et al., 1988; Ruderman, 1990; Yamauchi et al., 1997). A similarity of propagation of such waves with a harmonic oscillator was especially noted in (Ruderman, 1998). The HCS topology quite often assumes the presence of relatively small ripples in which from one to several SMIs occur with sizes of ~0.001–0.01 AU. The primary acceleration of energetic particles by magnetic reconnection at strong current sheets in the solar wind can reach hundreds of

keV, while trajectories of accelerated particles significantly depend on initial energies and the topology of the magnetic field around the neutral plane (Zharkova and Khabarova, 2012; 2015). In general, particles accelerated in this manner create clouds of different shapes around the current sheet. It is possible to identify angles and energies of the entry of pre-accelerated protons into a SMI only modeling specific situations observed in the solar wind, which currently goes beyond the scope of the problem we solve but is planned to be investigated in the future. Therefore, the "current sheet–SMI" system is extremely sensitive to topological factors which partly can be explained by the irregularity of detections of particles accelerated to MeV near current sheets in the solar wind.

Note that we also carried out calculations for the model of the electric and magnetic fields in an oscillating SMI in which the electric field is strictly orthogonal to the magnetic field. As expected, no average acceleration or deceleration is observed for such a configuration. However, the escape energy differs very little from the initial energy for the overwhelming majority of trajectories. The escape energy differs from the initial energy by more than 5% only for an insignificantly small fraction of the trajectories. Meantime, there is the most important population of particles with energies $0.7 < W_{\text{end}}/W^0 < 1.5$. This underlines the decisive role of the longitudinal electric field in the acceleration of charged particles.

CONCLUSIONS

A possibility of the additional acceleration of protons in an oscillating SMI trapped in the ripple of the HCS has been analyzed. It is assumed that protons are initially pre-accelerated by magnetic reconnection. The solar wind, energetic particle and magnetic/electric field parameters typical for crossings of the HCS at 1 AU are taken to simulate particle acceleration. It has been shown that the efficiency of the extra acceleration of protons depends on the initial injection energy, the size of an island, the oscillation phase, and the localization of the point to which pre-accelerated particles are injected.

For each "SMI size—initial energy—oscillation phase" configuration there is a set of points inside a SMI, injection to which leads to additional proton acceleration by an order of magnitude. Acceleration is weak or absent outside this region.

An interesting fact is that accelerated particles escaping from a SMI form an anisotropic cloud mainly in the equatorial region, directed towards the HCS. Physically, it means that these particles may subsequently be captured by the HCS and involved in the magnetic reconnection process over and over again. We will consider this scenario in the future. Note that observations also show signatures of anisotropy of energetic protons accelerated locally in the regions filled with SMIs (Khabarova et al., 2015a; 2015b; 2016).

The unequal efficiency of acceleration of particles with initially low and high energies is also a significant result. As noted in the Introduction, the acceleration mechanism for contraction/merging of SMIs proposed by (Zank et al., 2014) suggests that higher-energy particles are accelerated more effectively than lower-energy particles. This effect is indeed observed in the solar wind, but an inversion occurs below a certain threshold energy, and acceleration of the lowest-energy particles becomes most efficient. Our results show that, most likely, this is a manifestation of another mechanism of particle acceleration, namely the resonant pumping investigated in this study.

Summarizing, we have obtained the following main results, studying the behavior of particles in an oscillating SMI.

(1) A model of a SMI oscillating in the ripple of the reconnecting HCS with a period of several minutes is constructed. Different conditions of particle injection and SMI oscillation are considered. The modeling of extra acceleration of seed protons pre-accelerated to keV by magnetic reconnecting includes testing the system behavior at different phases of oscillations and suggests injection into different points inside a SMI. The maximum possible longitudinal electric field ($\sim 10^{-4}$–10^{-5} V/m) is taken for modeling. This opens a technical opportunity of describing the motion of particles in a single SMI within a configuration most favorable for particle behavior, imitating the particle acceleration in a system of a sufficiently large number of SMIs with smaller values of the longitudinal electric field.

(2) The modeling results show that a single oscillating in the background homogeneous magnetic field and the significant longitudinal inductive electric field can effectively accelerate charged particles pre-accelerated via another mechanism outside the SMI. The energy of accelerated protons can reach several MeV under favorable conditions.

(3) It can be suggested that resonant pumping effects arising from SMI oscillations are responsible for the previously observed phenomenon of the so-called "inversely ordered amplification factor" (Zank et al., 2015b) when particles with initially lower energies are accelerated more efficiently than particles with higher energies. As a result, all particles reach a certain energy threshold above which there is no acceleration. This cut-off energy appears to be at the level of 1–2 MeV for the system of SMIs in ripples of the HCS, which is consistent with observations (Khabarova et al., 2015a; 2015b; 2016; 2017). The stochastic mechanism at which particles with higher energies are accelerated (Zank et al., 2014; 2015a; 2015b) goes into action above this energy.

Therefore, the model of magnetic/electric fields in a SMI oscillating in the solar wind proposed in this

work reproduces some of known properties of energetic proton flux enhancements in the energy range from hundreds of keV to several MeV associated with SMIs near the HCS.

APPENDIX: METHOD FOR CALCULATING PROTON TRAJECTORIES

System of equations (47) and (48) should be represented in an optimal dimensionless (normalized) form to reduce computational costs and also for convenience. For this purpose, it is necessary to chose the scales $\hat{e} = |e|$, $\hat{m} = m_0$, $\hat{v} = c$, as well as the arbitrary value of any of the following scales: $\hat{t}, \hat{x}$, $\hat{B}$, $\hat{E}$, and determine the rest of them from the ratios $\hat{x} = c\hat{t}$, $\hat{t} = m_0/(e\hat{B})$, $\hat{E} = c\hat{B}$. As a result, if we denote the dimensionless charge by $e' = \mathrm{sign}(e) = \pm 1$ and traditionally denote the dimensionless impulse by $\mathbf{u}$:

$$\mathbf{u} = \mathbf{p}' = \mathbf{p}/(m_0 c) = \mathbf{v}\Big/\sqrt{1-|\mathbf{v}|^2/c^2} = \mathbf{v}'\Big/\sqrt{1-|\mathbf{v}'|^2},$$

then we obtain the following dimensionless forms of systems (48) and (49) (primes are omitted below):

$$\frac{d\mathbf{x}(t)}{dt} = \mathbf{v}(t), \quad \mathbf{u}(\mathbf{v}) = \frac{\mathbf{v}}{\sqrt{1-|\mathbf{v}|^2}},$$
$$\frac{d\mathbf{u}(\mathbf{v}(t))}{dt} = e'\left(\mathbf{E}(\mathbf{x}(t),t) + [\mathbf{v}(t)\times\mathbf{B}(\mathbf{x}(t),t)]\right), \tag{A.1}$$

$$\frac{d\mathbf{x}(t)}{dt} = \mathbf{v}(t), \quad \frac{d\mathbf{v}(t)}{dt} = e'\left(\mathbf{E}(\mathbf{x}(t),t) + [\mathbf{v}(t)\times\mathbf{B}(\mathbf{x}(t),t)]\right). \tag{A.2}$$

If the parameter $\beta = |\mathbf{v}|/c < \beta_0 = 0.02$ (which corresponds to the kinetic energy of $W_0 \approx 188$ keV) during the calculation of the trajectory, the time step within the classical system of equations (A.2) is used to save computational resources, and if a particle is accelerated at $\beta \geq \beta_0 = 0.02$, the time step within relativistic system of equations (A.1) is taken.

To solve the Cauchy problem (A.2), (50), at the initial part of the particle trajectory we use a method based on the exact solution of the problem for a nonrelativistic case for the electric and magnetic field constant in time and space, which was developed by us and showed a very high efficiency. This algorithm analytically takes into account rotation in the magnetic field, has no phase error, and removes the condition of the necessity of the sufficiently large number of time steps for calculations for the particle cyclotron rotation period. In the case of smoothly varying fields and a sufficiently strong magnetic field, the algorithm allows using a time step of tens or more cyclotron rotation periods, which makes it possible to significantly reduce computational costs. The algorithm developed by us has the second order accuracy, supports a variable time step, has explicit and implicit variants, and is based on the exact solution of the Cauchy problem (A.2), (50) for the case of $\mathbf{E} \equiv \mathrm{const}$, $\mathbf{B} \equiv \mathrm{const}$. This solution is shown below as a function of time and initial data in the notation of (53), using standard notations:

$$\mathbf{b} = \frac{\mathbf{B}}{|\mathbf{B}|}, \quad \mathbf{v}_E = \frac{[\mathbf{E}\times\mathbf{b}]}{|\mathbf{B}|}, \quad \omega_c = |\mathbf{B}|, \quad \mathbf{E}_\parallel = (\mathbf{E};\mathbf{b})\mathbf{b},$$
$$\mathbf{v}_\parallel = (\mathbf{v};\mathbf{b})\mathbf{b}, \quad \mathbf{v}_L = \mathbf{v} - \mathbf{v}_\parallel - \mathbf{v}_E, \quad \tau = t - t^0, \tag{A.3}$$

which can be represented as

$$\left.\begin{aligned}
&\mathbf{X}\left(t,t^0,\mathbf{x}^0,\mathbf{v}^0\right) = \mathbf{x}^0 + \left(\mathbf{v}_E + \mathbf{v}_\parallel^0\right)\tau + \frac{\tau^2}{2}e'\mathbf{E}_\parallel \\
&+ \frac{\mathbf{v}_L^0}{\omega_c}\sin(\omega_c\tau) - e'\frac{\left[\mathbf{b}\times\mathbf{v}_L^0\right]}{\omega_c}(1-\cos(\omega_c\tau)), \\
&\mathbf{V}\left(t,t^0,\mathbf{x}^0,\mathbf{v}^0\right) = \mathbf{v}_E + \mathbf{v}_\parallel^0 + \tau e'\mathbf{E}_\parallel \\
&+ \mathbf{v}_L^0\cos(\omega_c\tau) - e'\left[\mathbf{b}\times\mathbf{v}_L^0\right]\sin(\omega_c\tau).
\end{aligned}\right\} \tag{A.4}$$

Let us discuss the algorithm in terms of the layer-by-layer transition $t^0 \to t^1 = t^0 + \tau$ in the fields $\mathbf{E}(\mathbf{x},t)$ and $\mathbf{B}(\mathbf{x},t)$, given at any point at all times $t \geq t^0$. We denote $t^{1/2} = t^0 + \tau/2$, and introduce the notation $f^\alpha = f(t^\alpha)$ and $F^\alpha = F\left(\mathbf{x}(t^\alpha),t^\alpha\right)$, $\alpha = 0, \frac{1}{2}, 1$ for functions of the form of $f(t)$ and $F(\mathbf{x},t)$.

I. Starting iteration

I. 1. Find the fields $\mathbf{E}^0 = \mathbf{E}\left(\mathbf{x}^0,t^0\right)$, $\mathbf{B}^0 = \mathbf{B}\left(\mathbf{x}^0,t^0\right)$, after which one can find $\mathbf{b}^0$, $\mathbf{v}_E^0$, ω_c^0, $\mathbf{E}_\parallel^0 = \left(\mathbf{E}^0;\mathbf{b}^0\right)\mathbf{b}^0$, $\mathbf{v}_\parallel^0 = \left(\mathbf{v}^0;\mathbf{b}^0\right)\mathbf{b}^0$, $\mathbf{v}_L^0 = \mathbf{v}^0 - \mathbf{v}_\parallel^0 - \mathbf{v}_E^0$, using the obtained fields and (A.3).

I. 2. Find $\mathbf{x}^{1/2(0)} = \mathbf{X}\left(t^{1/2},t^0,\mathbf{x}^0,\mathbf{v}^0\right)$ in constant fields $\mathbf{E}^0,\mathbf{B}^0$ using the first formula in (A.4):

$$\mathbf{x}^{1/2(0)} = \mathbf{x}^0 + \left(\mathbf{v}_E^0 + \mathbf{v}_\parallel^0\right)\frac{\tau}{2} + \frac{\tau^2}{8}e'\mathbf{E}_\parallel^0 + \frac{\mathbf{v}_L^0}{\omega_c}\sin\left(\frac{\omega_c^0\tau}{2}\right) - e'\frac{\left[\mathbf{b}^0\times\mathbf{v}_L^0\right]}{\omega_c^0}\left(1-\cos\left(\frac{\omega_c^0\tau}{2}\right)\right).$$

Find $\mathbf{E}^{1/2(0)} = \mathbf{E}\left(\mathbf{x}^{1/2(0)},t^{1/2}\right)$, $\mathbf{B}^{1/2(0)} = \mathbf{B}\left(\mathbf{x}^{1/2(0)},t^{1/2}\right)$ and then find $\mathbf{b}^{1/2(0)}$, $\mathbf{v}_E^{1/2(0)}$, $\omega_c^{1/2(0)}$, $\mathbf{E}_\parallel^{1/2(0)} = \left(\mathbf{E}^{1/2(0)};\mathbf{b}^{1/2(0)}\right)\mathbf{b}^{1/2(0)}$, $\mathbf{v}_\parallel^{1/2(0)} = \left(\mathbf{v}^0;\mathbf{b}^{1/2(0)}\right)\mathbf{b}^{1/2(0)}$, $\mathbf{v}_L^{1/2(0)} = \mathbf{v}^0 - \mathbf{v}_\parallel^{1/2(0)} - \mathbf{v}_E^{1/2(0)}$, using the obtained fields and formulas (A.3).

I. 3. Find $\mathbf{x}^{1(0)} = \mathbf{X}\left(t^1, t^0, \mathbf{x}^0, \mathbf{v}^0\right)$ in constant fields $\mathbf{E}^{1/2(0)}$, $\mathbf{B}^{1/2(0)}$, using the first formula in (A.4)

$$\mathbf{x}^{1(\kappa)} = \mathbf{x}^0 + \left(\mathbf{v}_E^{1/2(\kappa)} + \mathbf{v}_\parallel^{1/2(\kappa)}\right)\tau + \frac{\tau^2}{2}e'\mathbf{E}_\parallel^{1/2(\kappa)} + \frac{\mathbf{v}_L^{1/2(\kappa)}}{\omega_c^{1/2(\kappa)}}\sin\left(\omega_c^{1/2(\kappa)}\tau\right) - e'\frac{\left[\mathbf{b}^{1/2(\kappa)} \times \mathbf{v}_L^{1/2(\kappa)}\right]}{\omega_c^{1/2(\kappa)}}\left(1 - \cos\left(\omega_c^{1/2(\kappa)}\tau\right)\right), \quad \text{(A.5)}$$

where $\kappa = 0$. Then, find fields $\mathbf{E}^{1(0)} = \mathbf{E}\left(\mathbf{x}^{1(0)}, t^1\right)$, $\mathbf{B}^{1(0)} = \mathbf{B}\left(\mathbf{x}^{1(0)}, t^1\right)$.

I. 4. Find $\mathbf{E}^{1/2(\kappa+1)} = \frac{1}{2}\left(\mathbf{E}^0 + \mathbf{E}^{1(\kappa)}\right)$, $\mathbf{B}^{1/2(\kappa+1)} = \frac{1}{2}\left(\mathbf{B}^0 + \mathbf{B}^{1(\kappa)}\right)$, for $\kappa = 0$. Next, use the obtained fields and formulas in (A.3) to find $\mathbf{b}^{1/2(\kappa+1)}$, $\mathbf{v}_E^{1/2(\kappa+1)}$, $\omega_c^{1/2(\kappa+1)}$, $\mathbf{E}_\parallel^{1/2(\kappa+1)}$, $\mathbf{v}_\parallel^{1/2(\kappa+1)} = \left(\mathbf{v}^0; \mathbf{b}^{1/2(\kappa+1)}\right)\mathbf{b}^{1/2(\kappa+1)}$, $\mathbf{v}_L^{1/2(\kappa+1)} = \mathbf{v}^0 - \mathbf{v}_\parallel^{1/2(\kappa+1)} - \mathbf{v}_E^{1/2(\kappa+1)}$. Then, find $\mathbf{x}^{1(1)} = \mathbf{X}\left(t^1, t^0, \mathbf{x}^0, \mathbf{v}^0\right)$ in constant fields $\mathbf{E}^{1/2(1)}$, $\mathbf{B}^{1/2(1)}$ for $\kappa = 1$, using Eq. (A.5). Next, find the fields $\mathbf{E}^{1(1)} = \mathbf{E}\left(\mathbf{x}^{1(1)}, t^1\right)$, $\mathbf{B}^{1(1)} = \mathbf{B}\left(\mathbf{x}^{1(1)}, t^1\right)$ as well as the accuracy parameter $\delta_1 = \left\|\mathbf{x}^{1(1)} - \mathbf{x}^{1(0)}\right\|$. If the specified accuracy δ: $\delta_1 \le \delta$ is reached, then the process is complete. Otherwise, a regular iteration is performed.

II. Regular iteration $\kappa \to \kappa + 1$. Find $\mathbf{x}^{1(\kappa+1)}$, $\mathbf{E}^{1(\kappa+1)}$, $\mathbf{B}^{1(\kappa+1)}$ as well as the relative accuracy parameter $\delta_{\kappa+1} = \left\|\mathbf{x}^{1(\kappa+1)} - \mathbf{x}^{1(\kappa)}\right\|$ and the convergence parameter $\gamma_{\kappa+1} = \delta_{\kappa+1} - \delta_\kappa$ by performing actions described in **I. 4.**, using the obtained $\mathbf{x}^{1(\kappa)}$, $\mathbf{E}^{1(\kappa)}$, $\mathbf{B}^{1(\kappa)}$. Iterations are performed until the specified relative accuracy $\delta_{\kappa+1} \le \delta$ is reached. If the convergence condition of the process $\gamma_{\kappa+1} = \delta_{\kappa+1} - \delta_\kappa < 0$ is violated at a certain iteration, or if the number of iterations exceeds the specified maximum allowable number κ_0, then the current time step τ is halved: $\tau \to \tau/2$, and the described process starts all over again.

III. Step completion unit. Set $\mathbf{x}^1 = \mathbf{x}^{1(\kappa+1)}$, $\mathbf{E}^1 = \mathbf{E}^{1(\kappa+1)}$, $\mathbf{B}^1 = \mathbf{B}^{1(\kappa+1)}$. Then find the fields $\mathbf{E}^{1/2} = \frac{1}{2}\left(\mathbf{E}^0 + \mathbf{E}^1\right)$, $\mathbf{B}^{1/2} = \frac{1}{2}\left(\mathbf{B}^0 + \mathbf{B}^1\right)$. Next, use the obtained fields and the formulas from (A.3) to find $\mathbf{b}^{1/2}$, $\mathbf{v}_E^{1/2}$, $\omega_c^{1/2}$, $\mathbf{E}_\parallel^{1/2}$, $\mathbf{v}_\parallel^{1/2} = \left(\mathbf{v}^0; \mathbf{b}^{1/2}\right)\mathbf{b}^{1/2}$, $\mathbf{v}_L^{1/2} = \mathbf{v}^0 - \mathbf{v}_\parallel^{1/2} - \mathbf{v}_E^{1/2}$. Then, find $\mathbf{v}^1 = \mathbf{V}\left(t, t^0, \mathbf{x}^0, \mathbf{v}^0\right)$ in constant fields $\mathbf{E}^{1/2}$, $\mathbf{B}^{1/2}$ by the second formula in (A.4)

$$\mathbf{v}^1 = \mathbf{v}_E^{1/2} + \mathbf{v}_\parallel^{1/2} + \tau e'\mathbf{E}_\parallel^{1/2} + \mathbf{v}_L^{1/2}\cos\left(\omega_c^{1/2}\tau\right) - e'\left[\mathbf{b}^{1/2} \times \mathbf{v}_L^{1/2}\right]\sin\left(\omega_c^{1/2}\tau\right).$$

The time step is over at this point.

The authors have developed an implicit scheme of the second order of accuracy to solve the Cauchy problem (A.1), (50) numerically in the relativistic case. It is necessary to introduce the following function to formulate the problem in terms of the layer-by-layer transition $t^0 \to t^1 = t^0 + \tau$

$$\Gamma(\mathbf{u}) = \frac{1}{\gamma(\mathbf{v})} = \frac{1}{\sqrt{1 + |\mathbf{u}|^2}} = \sqrt{1 - |\mathbf{v}|^2}, \quad \text{(A.6)}$$

and present system (64) as follows

$$\frac{d\mathbf{x}(t)}{dt} = \Gamma(\mathbf{u}(t))\,\mathbf{u}(t), \quad \frac{d\mathbf{u}(t)}{dt} = e'\left(\mathbf{E}(\mathbf{x}(t), t) + \Gamma(\mathbf{u}(t))\left[\mathbf{u}(t) \times \mathbf{B}(\mathbf{x}(t), t)\right]\right), \quad \text{(A.7)}$$

and use the following equations arising from it:

$$\frac{d\Gamma(\mathbf{u}(t))}{dt} = -e'\left(\Gamma(\mathbf{u}(t))\right)^3\left(\mathbf{u}(t); \mathbf{E}(\mathbf{x}(t), t)\right), \quad \text{(A.8)}$$

$$\frac{d^2\mathbf{x}(t)}{dt^2} = e'\Gamma(\mathbf{u}(t))\left(\mathbf{E}(\mathbf{x}(t), t) + \Gamma(\mathbf{u}(t))\left[\mathbf{u}(t) \times \mathbf{B}(\mathbf{x}(t), t)\right]\right) + \frac{d\Gamma(\mathbf{u}(t))}{dt}\mathbf{u}(t). \quad \text{(A.9)}$$

The scheme is based on the following finite difference relations:

$$\frac{\mathbf{x}^1 - \mathbf{x}^0}{\tau} = \frac{1}{2}\left(\Gamma^0\mathbf{u}^0 + \Gamma^1\mathbf{u}^1\right) - \frac{\tau}{12}\left(\left(\frac{d^2\mathbf{x}}{dt^2}\right)^1 - \left(\frac{d^2\mathbf{x}}{dt^2}\right)^0\right) + O\left(\tau^4\right), \quad \text{(A.10)}$$

$$\frac{\mathbf{u}^1 - \mathbf{u}^0}{\tau} = \frac{1}{2}\left(\left(\frac{d\mathbf{u}}{dt}\right)^0 + \left(\frac{d\mathbf{u}}{dt}\right)^1\right) + O\left(\tau^2\right), \quad \text{(A.11)}$$

I. Starting iteration.

I. 1. Find $\mathbf{E}^0 = \mathbf{E}\left(\mathbf{x}^0, t^0\right)$, $\mathbf{B}^0 = \mathbf{B}\left(\mathbf{x}^0, t^0\right)$, and then use the obtained fields and formulas (A.6)–(A.9) to find $\left(\frac{d\mathbf{u}}{dt}\right)^0$, $\left(\frac{d\Gamma}{dt}\right)^0$, $\left(\frac{d^2\mathbf{x}}{dt^2}\right)^0$.

I. 2. Find $\mathbf{x}^{1(0)}$ with an accuracy of $O(\tau^3)$ and $\Gamma^{1(-)}$ with an accuracy of $O(\tau^2)$, using the following extrapolations:

$$\mathbf{x}^{1(0)} = \mathbf{x}^0 + \tau\Gamma^0\mathbf{u}^0 + \frac{\tau^2}{2}\left(\frac{d^2\mathbf{x}}{dt^2}\right)^0 + O(\tau^3),$$
$$\Gamma^{1(-)} = \Gamma^0 + \tau\left(\frac{d\Gamma}{dt}\right)^0 + O(\tau^2).$$

Next, find $\mathbf{E}^{1(0)} = \mathbf{E}\left(\mathbf{x}^{1(0)}, t^1\right)$, $\mathbf{B}^{1(0)} = \mathbf{B}\left(\mathbf{x}^{1(0)}, t^1\right)$ with an accuracy of $O(\tau^3)$, using $\mathbf{x}^{1(0)}$.

I. 3. Find $\mathbf{u}^{1(0)}$ with an accuracy of $O(\tau^3)$ as follows. One can obtain the following vector equation for $\mathbf{u}^1$: from (A.11) and the second equation in (A.7)

$$\left.\begin{array}{l}\mathbf{u}^1 + \dfrac{\tau}{2}e'\Gamma^1\left[\mathbf{B}^1\times\mathbf{u}^1\right] = \mathbf{W} + O(\tau^3), \quad \text{where}\\ \mathbf{W} = \mathbf{W}^0 + \mathbf{W}^1, \ \mathbf{W}^0 = \mathbf{u}^0 + \dfrac{\tau}{2}\left(\dfrac{d\mathbf{u}}{dt}\right)^0,\\ \mathbf{W}^1 = \dfrac{\tau}{2}e'\mathbf{E}^1.\end{array}\right\} \quad \text{(A.12)}$$

This equation can be represented in the form of a system of linear equations with the matrix $(\hat{\mathbf{I}} + \hat{\boldsymbol{\omega}})$:

$$\left(\hat{\mathbf{I}} + \hat{\boldsymbol{\omega}}\right)\mathbf{u} = \mathbf{W},$$
$$\text{where } \hat{\mathbf{I}} \text{ is the identity matrix and} \quad \hat{\boldsymbol{\omega}}\mathbf{u} = [\boldsymbol{\omega}\times\mathbf{u}]. \quad \text{(A.13)}$$

The inverse matrix $(\hat{\mathbf{I}} + \hat{\boldsymbol{\omega}})^{-1}$ has the following form

$$(\hat{\mathbf{I}} + \hat{\boldsymbol{\omega}})^{-1} = \frac{1}{1+|\boldsymbol{\omega}|^2}(\hat{\mathbf{I}} - \hat{\boldsymbol{\omega}} + \boldsymbol{\omega}\otimes\boldsymbol{\omega}), \text{ where}$$

$\boldsymbol{\omega}\otimes\boldsymbol{\omega}$ is the dyad formed by the vector $\boldsymbol{\omega}$.

Therefore, the solution of vector equation (A.13) is given by the following formula

$$\mathbf{u} = (\hat{\mathbf{I}} + \hat{\boldsymbol{\omega}})^{-1}\mathbf{W} = \frac{1}{1+|\boldsymbol{\omega}|^2}(\mathbf{W} - [\boldsymbol{\omega}\times\mathbf{W}] + (\mathbf{W};\boldsymbol{\omega})\boldsymbol{\omega}). \quad \text{(A.14)}$$

We obtain an expression for $\mathbf{u}^1$ through the remaining terms by applying this formula to Eq. (A.13) for $\boldsymbol{\omega} = \frac{\tau}{2}\Gamma^1\mathbf{B}^1$,

$$\mathbf{u}^1 = \frac{\mathbf{W} - \frac{\tau}{2}e'\Gamma^1\left[\mathbf{B}^1\times\mathbf{W}\right] + \left(\frac{\tau}{2}\Gamma^1\right)^2\left(\mathbf{W};\mathbf{B}^1\right)\mathbf{B}^1}{\left(1+\left(\frac{\tau}{2}\Gamma^1|\mathbf{B}^1|\right)^2\right)} + O(\tau^3). \quad \text{(A.15)}$$

We obtain the following formulas by substituting the already found $\Gamma^{1(-)}$, $\mathbf{B}^{1(0)}$, $\mathbf{E}^{1(0)}$, into this formula:

$$\left.\begin{array}{c}\mathbf{W} = \mathbf{W}^0 + \mathbf{W}^{1(0)}, \quad \mathbf{W}^{1(0)} = \dfrac{\tau}{2}e'\mathbf{E}^{1(0)},\\ \mathbf{u}^{1(0)} = \dfrac{\mathbf{W} - \frac{\tau}{2}e'\Gamma^{1(-)}\left[\mathbf{B}^{1(0)}\times\mathbf{W}\right] + \left(\frac{\tau}{2}\Gamma^{1(-)}\right)^2\left(\mathbf{W};\mathbf{B}^{1(0)}\right)\mathbf{B}^{1(0)}}{\left(1+\left(\frac{\tau}{2}\Gamma^{1(-)}\left|\mathbf{B}^{1(0)}\right|\right)^2\right)} + O(\tau^3).\end{array}\right\} \quad \text{(A.16)}$$

I. 4. Find $\Gamma^{1(0)}$ by formula (A.6) using the obtained $\mathbf{u}^{1(0)}$ and $\mathbf{B}^{1(0)}$, $\mathbf{E}^{1(0)}$, with the accuracy of $O(\tau^3)$ as well as $\left(\frac{d\mathbf{u}}{dt}\right)^{1(0)}$ by formula (A.7) and $\left(\frac{d^2\mathbf{x}}{dt^2}\right)^{1(0)}$ by formula (A.9). Assign $\delta_0 = 1$.

II. Regular iteration $\kappa \to \kappa+1$. Let $\mathbf{x}^{1(\kappa)}$, $\mathbf{u}^{1(\kappa)}$, $\Gamma^{1(\kappa)}$, $\mathbf{B}^{1(\kappa)}$, $\mathbf{E}^{1(\kappa)}$, $\left(\frac{d\mathbf{u}}{dt}\right)^{1(\kappa)}$, $\left(\frac{d^2\mathbf{x}}{dt^2}\right)^{1(\kappa)}$ be known with an accuracy of $O(\tau^3)$.

II. 1. Find $\mathbf{x}^{1(\kappa+1)}$ with the accuracy of $O(\tau^4)$ from relation (A.10):

$$\mathbf{x}^{1(\kappa+1)} = \mathbf{x}^0 + \frac{\tau}{2}\left(\Gamma^0\mathbf{u}^0 + \Gamma^{1(\kappa)}\mathbf{u}^{1(\kappa)}\right) - \frac{\tau^2}{12}\left(\left(\frac{d^2\mathbf{x}}{dt^2}\right)^{1(\kappa)} - \left(\frac{d^2\mathbf{x}}{dt^2}\right)^0\right) + O\left(\tau^4\right).$$

Next, find $\mathbf{E}^{1(\kappa+1)} = \mathbf{E}\left(\mathbf{x}^{1(\kappa+1)}, t^1\right)$, $\mathbf{B}^{1(\kappa+1)} = \mathbf{B}\left(\mathbf{x}^{1(\kappa+1)}, t^1\right)$ with the accuracy of $O(\tau^4)$.

II. 2. Find $\mathbf{u}^{l(\kappa+1)}$ with the accuracy of $O(\tau^3)$, using formula (A.11) completely similar to finding (A.16):

$$\mathbf{W} = \mathbf{W}^0 + \mathbf{W}^{l(\kappa+1)}, \quad \mathbf{W}^{l(\kappa+1)} = \frac{\tau}{2} e' \mathbf{E}^{l(\kappa+1)},$$
$$\mathbf{u}^{l(\kappa+1)} = \frac{\mathbf{W} - \frac{\tau}{2} e' \Gamma^{l(\kappa)} \left[\mathbf{B}^{l(\kappa+1)} \times \mathbf{W} \right] + \left(\frac{\tau}{2} \Gamma^{l(\kappa)} \right)^2 \left(\mathbf{B}^{l(\kappa+1)}; \mathbf{W} \right) \mathbf{B}^{l(\kappa+1)}}{\left(1 + \left(\frac{\tau}{2} \Gamma^{l(\kappa)} \left| \mathbf{B}^{l(\kappa+1)} \right| \right)^2 \right)} + O(\tau^3).$$

II. 3. Find $\Gamma^{l(\kappa+1)}$, employing formula (A.6) and using the obtained $\mathbf{u}^{l(\kappa+1)}$ and $\mathbf{B}^{l(\kappa+1)}$, $\mathbf{E}^{l(\kappa+1)}$ with the accuracy $O(\tau^3)$ as well as $\left(\frac{d\mathbf{u}}{dt}\right)^{l(\kappa+1)}$, using formula (A.7) and $\left(\frac{d^2\mathbf{x}}{dt^2}\right)^{l(\kappa+1)}$, using formula (A.9).

II. 4. Find the relative accuracy parameter $\delta_{\kappa+1} = \left\| \mathbf{x}^{l(\kappa+1)} - \mathbf{x}^{l(\kappa)} \right\|$ and the convergence parameter $\gamma_{\kappa+1} = \delta_{\kappa+1} - \delta_\kappa$. Iterations are performed until the specified relative accuracy is reached $\delta_{\kappa+1} \le \delta$. If the convergence condition of the iteration process $\gamma_{\kappa+1} = \delta_{\kappa+1} - \delta_\kappa < 0$ is violated at some iteration or the number of iterations exceeds the specified maximum allowable number κ_0, then the current time step τ is halved, $\tau \to \tau/2$, and the iteration process starts over. At the end, perform the following assignment $\mathbf{x}^1 = \mathbf{x}^{l(\kappa+1)}$, $\mathbf{u}^1 = \mathbf{u}^{l(\kappa+1)}$, $\Gamma^1 = \Gamma^{l(\kappa+1)}$, $\mathbf{E}^1 = \mathbf{E}^{l(\kappa+1)}$, $\mathbf{B}^1 = \mathbf{B}^{l(\kappa+1)}$, $\left(\frac{d\mathbf{u}}{dt}\right)^1 = \left(\frac{d\mathbf{u}}{dt}\right)^{l(\kappa+1)}$, $\left(\frac{d^2\mathbf{x}}{dt^2}\right)^1 = \left(\frac{d^2\mathbf{x}}{dt^2}\right)^{l(\kappa+1)}$.

Note that the described algorithm for solving the Cauchy problem (49), (50) in the nonrelativistic case has been widely used since 2000 (see, for example, Borodachev et al., 2003; Mingalev et al., 2006; 2007; 2009; 2012; Malova et al., 2015), thoroughly tested and proved its correctness and effectiveness in practice. Therefore, it is necessary to test only the new implicit scheme for the relativistic case. The exact solution of the Cauchy problem (47), (50) is best suited for this testing in the case of constant magnetic and electric fields parallel to each other when a charged particle is accelerated by the electric field. Note that this solution was discussed in (Landau and Lifshits, 2012), but only a special case in which the initial charge velocity is orthogonal to the magnetic field was considered there. Also, an unsuitable parametrization which gives only an implicit relation for the solution and does not allow to obtain a solution explicitly was chosen by (Landau and Lifshits, 2012). The authors could not find the discussed exact solution in available literature sources. Therefore, we have obtained the solution ourselves in an explicit vector form and for arbitrary initial conditions.

Let us consider the Cauchy problem for dimensionless system (A.6), (A.7) in the case of constant and parallel fields $\mathbf{B} \equiv \text{const}$, $\mathbf{E} \equiv E_\parallel \mathbf{b} \equiv \text{const}$ (where $\mathbf{b} = \mathbf{B}/|\mathbf{B}|$). It can be represented as follows

$$\frac{d\mathbf{x}(t)}{dt} = \frac{\mathbf{u}(t)}{\sqrt{1 + |\mathbf{u}(t)|^2}},$$
$$\frac{d\mathbf{u}(t)}{dt} = e' \left(E_\parallel \mathbf{b} + \frac{[\mathbf{u}(t) \times \mathbf{B}]}{\sqrt{1 + |\mathbf{u}(t)|^2}} \right), \qquad (A.17)$$
$$\mathbf{x}(t^0) = \mathbf{x}^0, \ \mathbf{u}(t^0) = \mathbf{u}^0.$$

Let us denote

$$\Gamma(\mathbf{u}) = \sqrt{1 + |\mathbf{u}|^2} = \frac{1}{\sqrt{1 - |\mathbf{v}|^2}}, \ u_\parallel = (\mathbf{u}; \mathbf{b}), \qquad (A.18)$$
$$\mathbf{u}_\parallel = (\mathbf{u}; \mathbf{b})\mathbf{b}, \ \mathbf{u}_\perp = \mathbf{u} - \mathbf{u}_\parallel, \ \tau = t - t^0.$$

It is convenient to present the exact solution of problem (A.17) obtained by us in the following form. We obtain the following formula for the Lorentz factor

$$\Gamma(\mathbf{u}) = \gamma(\tau) = \sqrt{1 + \left|\mathbf{u}_\perp^0\right|^2 + \left(u_\parallel^0 + e' E_\parallel \tau\right)^2}$$
$$= \sqrt{\left(\gamma^0\right)^2 + e' E_\parallel \tau \left(2u_\parallel^0 + e' E_\parallel \tau\right)}, \qquad (A.19)$$
$$\text{where} \quad \gamma^0 = \sqrt{1 + |\mathbf{u}^0|^2}.$$

The following formulas are obtained for the cyclotron rotation phase

$$\frac{d\Phi(\tau)}{d\tau} = \frac{|\mathbf{B}|}{\gamma(\tau)},$$
$$\Phi(\tau) = e' \frac{|\mathbf{B}|}{E_\parallel} \ln \left(\frac{u_\parallel^0 + e' E_\parallel \tau + \gamma(\tau)}{u_\parallel^0 + \gamma^0} \right). \qquad (A.20)$$

For a dimensionless impulse, we obtain a formula similar to the formula for the velocity in (A.4):

$$\mathbf{u}(t) = \mathbf{u}_\parallel^0 + e' E_\parallel \tau \mathbf{b} +$$
$$+ \mathbf{u}_\perp^0 \cos(\Phi(\tau)) - e' \left[\mathbf{b} \times \mathbf{u}_\perp^0 \right] \sin(\Phi(\tau)). \qquad (A.21)$$

The following formula is obtained for the coordinate

$$\mathbf{x}(t) = \mathbf{x}^0 + \frac{e'}{E_\parallel}\left(\gamma(\tau) - \gamma^0\right)\mathbf{b} + \frac{\mathbf{u}_\perp^0}{|\mathbf{B}|}\sin(\Phi(\tau)) - e'\frac{\left[\mathbf{b}\times\mathbf{u}_\perp^0\right]}{|\mathbf{B}|}(1-\cos(\Phi(\tau))). \quad (A.22)$$

Calculations were carried out for solving the Cauchy problem (A.17), using the implicit second-order scheme (A.10), (A.11) described above in a wide range of relativistic initial conditions and parameter values $E_\parallel/|\mathbf{B}|$ for the time $T = 40\Theta_0$, where $\Theta_0 = 2\pi\Big/\frac{d\Phi(0)}{d\tau} = \frac{2\pi\gamma^0}{|\mathbf{B}|}$. These calculations showed that in the case of a sufficiently small time step, the numerical solution corresponds to the exact solution of (A.19)–(A.22) with a high accuracy.

AKCNOWLEDGMENTS

This work was supported by the subprogram V.15 Dynamics of a Rarefied Plasma in Space and Laboratory of the Integrated Program for Basic Research of the Division of Physical Sciences of the Russian Academy of Sciences. Kh.V. Malova was supported by the Russian Science Foundation, project no. 14-12-00824. O.V. Mingalev, I.V. Mingalev, and O.V. Khabarova acknowledge the support of the Russian Foundation for Basic Research, project nos. 16-02-00479, 17-02-00300, 17-02-01328, 18-52-06002, and 19-02-00957. G.P. Zank acknowledges the partial support of the NSF EPSCoR RII-Track-1 Cooperative Agreement OIA-1655280, NSF-DOE award 1707247. We are grateful to the SMEI and STELab data processing groups for the 3D reconstruction of the density, the speed, and the magnetic field patterns in the heliosphere (data from http://smei.ucsd.edu/new_smei/data&images/data&images.html were used).

REFERENCES

Bemporad, A., Spectroscopic detection of turbulence in post-CME current sheets, *Astrophys. J.*, 2008, vol. 689, no. 1, pp. 572–584. doi 10.1086/592377

Bian, N.H. and Kontar, E.P., Stochastic acceleration by multi-island contraction during turbulent magnetic reconnection, *Phys. Rev. Lett.*, 2013, vol. 110, no. 15, art. ID 151101. doi 10.1103/PhysRevLett.110.151101

Borodachev, L.V., Mingalev, I.V., and Mingalev, O.V., Algorithm for simulating the drift motion of a particle in plasma described by the Darwin model, *Comput. Math. Math. Phys.*, 2003, vol. 43, no. 3, pp. 446–458.

Cartwright, M.L. and Moldwin, M.B., Comparison of small-scale flux rope magnetic properties to large-scale magnetic clouds: Evidence for reconnection across the HCS? *J. Geophys. Res.: Space Phys.*, 2008, vol. 113, no. 9, art. ID A09105. doi 10.1029/2008JA013389

Dai, L., Wygant, J.R., Cattel, C.A., Thaller, S., Kersten, K., Breneman, A., and Tang, X., Cluster observations of fast magnetosonic waves in the heliospheric current sheet, *Geophys. Res. Lett.*, 2014, vol. 41, pp. 1398–1405. doi 10.1002/2014GL059223

Drake, J.F., Swisdak, M., Che, H., and Shay, M.A., Electron acceleration from contracting magnetic islands during reconnection, *Nature*, 2006, vol. 433, no. 7111, pp. 553–556. doi 10.1038/nature05116

Eastwood, J.P., Balogh, A., Dunlop, M.W., and Smith, C.W., Cluster observations of the heliospheric current sheet and an associated magnetic flux rope and comparisons with ACE, *J. Geophys. Res.: Space Phys.*, 2002, vol. 107, no. 11, pp. SSH 9-1–SSH 9-9. doi 10.1029/2001JA009158

Greco, A., Perri, S., Servidio, S., Yordanova, E., and Veltri, P., The complex structure of magnetic field discontinuities in the turbulent solar wind, *Astrophys. J. Lett.*, 2016, vol. 823, no. 2, art. ID L39. doi 10.3847/2041-8205/823/2/L39

Khabarova, O., Zank, G.P., Li, G., le Roux, J.A., Webb, G.M., Dosch, A. and Malandraki, O.E., Small-scale magnetic islands in the solar wind and their role in particle acceleration. I. Dynamics of magnetic islands near the heliospheric current sheet, *Astrophys. J.*, 2015a, vol. 808, no. 2, art. ID 181. doi 10.1088/0004-637X/808/2/181

Khabarova, O., Zank, G.P., Li, G., le Roux, J.A., Webb, G.M., Malandraki, O.E. and Zharkova, V.V., Dynamical small-scale magnetic islands as a source of local acceleration of particles in the solar wind, *J. Phys.: Conf. Ser.*, 2015b, vol. 642, art. ID 012033. doi 10.1088/1742-6596/642/1/012033

Khabarova, O., Zank, G.P., Li, G., Malandraki, O.E., le Roux, J.A., Webb, G.M., and Dosch, A., Small-scale magnetic islands in the solar wind and their role in particle acceleration. II. Particle energization inside magnetically confined cavities, *Astrophys. J.*, 2016, vol. 827, no. 2, art. ID 122. doi 10.3847/0004-637X/827/2/122

Khabarova, O.V., Zank, G.P., Malandraki, O.E., Li, G., le Roux, J.A., and Webb, G.M., Observational evidence for local particle acceleration associated with magnetically confined magnetic islands in the heliosphere—a review, *Sun Geosphere*, 2017, vol. 12, no. 1, pp. 23–30.

Landau, L.D. and Lifshitz, E.M., *A Course of Theoretical Physics*, Vol. 2: *The Classical Theory of Fields*, New York: Pergamon, 1971.

le Roux, J.A., Zank, G.P., Webb, G.M., and Khabarova, O.A., Energetic ion acceleration by small-scale solar wind flux ropes, *Astrophys. J.*, 2015, vol. 801, no. 2, art. ID 112. doi 10.1088/0004-637X/801/2/112

le Roux, J.A., Zank, G.P., Webb, G.M., and Khabarova, O.V., Kinetic transport theory for particle acceleration and transport in regions of multiple contracting and reconnecting inertial-scale flux ropes, *Astrophys. J.*, 2016, vol. 827, no. 1, art. ID 47. doi 10.3847/0004-637X/827/1/47

Lifshitz, E.M. and Pitaevskii, L.P., *Course of Theoretical Physics*, Vol. 10: *Physical Kinetics*, Amsterdam: Elsevier, 1981.

Malova, H.V., Mingalev, O.V., Grigorenko, E.E., Mingalev, I.V., Melnik, M.N., Popov, V.Yu., Delcourt, D.C., Petrukovich, A.A., Shen, C., Rong, D., and Zelenyi, L.M.,

Formation of self-organized shear structures in thin current sheets, *J. Geophys. Res.: Space Phys.*, 2015, vol. 120. doi 10.1002/2014JA020974

Markidis, S., Henri, P., Lapenta, G., Divin, A., Goldman, M., Newman, D., and Laure, E., Kinetic simulations of plasmoid chain dynamics, *Phys. Plasmas*, 2013, vol. 20, no. 8, art. ID 082105. http://dx.doi.org/10.1063/1.4817286

Matthaeus, W.H., Ambrosiano, J.J., and Goldstein, M.L., Particle acceleration by turbulent magnetohydrodynamic reconnection, *Phys. Rev. Lett.*, 1984, vol. 53, pp. 1449–1452. doi 10.1103/PhysRevLett.53.1449

Merkin, V.G., Lyon, J.G., McGregor, S.L., and Pahud, D.M., Disruption of a heliospheric current sheet fold, *Geophys. Res. Lett.*, 2011, vol. 38, art. ID L14107. doi 10.1029/2011GL047822

Mingalev, O.V., Mingalev, I.V., and Mingalev, V.S., Two-dimensional numerical simulation of dynamics of small-scale irregularities in the near-Earth plasma, *Cosmic Res.*, 2006, vol. 44, no. 5, pp. 398–408.

Mingalev, O.V., Mingalev, I.V., Malova, Kh.V., and Zelenyi, L.M., Numerical simulations of plasma equilibrium in a one-dimensional current sheet with a nonzero normal magnetic field component, *Plasma Phys. Rep.*, 2007, vol. 33, no. 11, pp. 942–955.

Mingalev, O.V., Mingalev, I.V., Malova, Kh.V., Zelenyi, L.M., and Artem'ev, A.V., Asymmetric configurations of a thin current sheet with a constant normal magnetic field component, *Plasma Phys. Rep.*, 2009, vol. 35, no. 1, pp. 76–83.

Mingalev, O.V., Mingalev, I.V., Mel'nik, M.N., Artemyev, A.V., Malova, H.V., Popov, V.Y., Chao, S., and Zelenyi, L.M., Kinetic models of current sheets with a sheared magnetic field, *Plasma Phys. Rep.*, 2012, vol. 38, no. 4, pp. 300–314.

Musielak, Z.E. and Suess, S.T., Magnetohydrodynamic bending waves in a current sheet, *Sol. Phys.*, 1988, vol. 330, pp. 456–465. doi 10.1086/166483

Oka, M., Phan, T.-D., Krucker, S., Fujimoto, M., and Shinohara, I., Electron acceleration by multi-island coalescence, *Astrophys. J.*, 2010, vol. 714, no. 1, pp. 915–926. doi 10.1088/0004-637X/714/1/915

Ruderman, M.S., Nonlinear surface wave propagation on heliospheric current sheet, *Proc. Ist COSPAR Colloquium "Physics of the Outer Heliosphere," Warsaw, Poland*, Oxford: Pergamon, 1990, vol. 1, pp. 249–252. doi 10.1016/B978-0-08-040780-7.50046-410.1016/B978-0-08-040780-7.50046-4

Ruderman, M.S., On the analogy between a system of harmonic oscillators and resonant Alfven waves in plasmas, *Phys. Plasmas*, 1998, vol. 5, no. 6, pp. 2463–2465. doi 10.1063/1.872927

Wang, S., Lee, L.C., Wei, C.Q., and Akasofu, S.-I., A mechanism for the formation of plasmoids and kink waves in the heliospheric current sheet, *Sol. Phys.*, 1988, vol. 117, pp. 157–169.

Yamauchi, M. and Lui, A.T.Y., Modified magnetohydrodynamic waves in a current sheet in space, *Phys. Plasmas*, 1997, vol. 4, no. 12, pp. 4382–4387. doi 10.1063/1.872600

Zank, G.P., le Roux, J.A., Webb, G.M., Dosch, A., and Khabarova, O., Particle acceleration via reconnection processes in the supersonic solar wind, *Astrophys. J.*, 2014, vol. 797, no. 1. doi 10.1088/0004-637X/797/1/28

Zank, G.P., Hunana, P., Mostafavi, P., le Roux, J.A., Li, G., Webb, G.M., and Khabarova, O.V., Particle acceleration by combined diffusive shock acceleration and downstream multiple magnetic island acceleration, *J. Phys.: Conf. Ser.*, 2015a, vol. 642, no. 1, art. ID 012031. doi. http://iopscience.iop.org/1742-6596/642/1/012031.10.1088/1742-6596/642/1/012031

Zank, G.P., Hunana, P., Mostafavi, P., le Roux, J.A., Li, G., Webb, G.M., Khabarova, O., Cummings, A., Stone, E., and Decker, R., Diffusive shock acceleration and reconnection acceleration processes, *Astrophys. J.*, 2015b, vol. 814, no. 2, art. ID 137. doi 10.1088/0004-637X/814/2/137

Zharkova, V. and Khabarova, O., Particle acceleration in the reconnecting heliospheric current sheet: solar wind data versus 3D PIC simulations, *Astrophys. J.*, 2012, vol. 752, no. 1, art. ID 35. doi 10.1088/0004-637X/752/1/35

Zharkova, V. and Khabarova, O., Additional acceleration of solar-wind particles in current sheets of the heliosphere, *Ann. Geophys.*, 2015, vol. 33, no. 457, pp. 457–470. doi 10.5194/angeo-33-457-2015

Zheng, J. and Hu, Q., Observational evidence for self-generation of small-scale magnetic flux ropes from intermittent solar wind turbulence, *Astrophys. J. Lett.*, 2018, vol. 852, no. 2, art. ID L23. doi 10.3847/2041-8213/aaa3d7

Zhou, X., Büchner, J., Bárta, M., Gan, W., and Liu, S., Electron acceleration by cascading reconnection in the solar corona. I. Magnetic gradient and curvature drift effects, *Astrophys. J.*, 2015, vol. 815, no. 1, art. ID 6. doi 10.1088/0004-637X/815/1/6

Translated by O. Pismenov